

**CONVECTIVE VARIABILITY ASSOCIATED WITH A MESOSCALE  
VORTEX IN A MIDLATITUDE SQUALL LINE SYSTEM**

A Thesis

by

**SVETLA MIHAYLOVA HRISTOVA-VELEVA**

Submitted to the Office of Graduate Studies of  
Texas A&M University  
in partial fulfillment of the requirements for the degree of

**MASTER OF SCIENCE**

May 1994

Major Subject: Meteorology

CONVECTIVE VARIABILITY ASSOCIATED WITH A MESOSCALE  
VORTEX IN A MIDLATITUDE SQUALL LINE SYSTEM

A Thesis

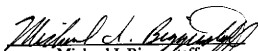
by

SVETLA MIHAYLOVA HRISTOVA-VELEVA

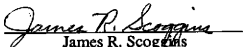
Submitted to Texas A&M University  
in partial fulfillment of the requirements  
for the degree of

MASTER OF SCIENCE

Approved as to style and content by:



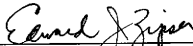
Michael I. Biggerstaff  
(Chair of Committee)



James R. Scoggins  
(Member)



Juan B. Valdes  
(Member)



Edward J. Zipser  
(Head of Department)

May 1994

Major Subject: Meteorology

**ABSTRACT****Convective Variability Associated with a Mesoscale Vortex in a Midlatitude Squall Line System. (May 1994)**

**Svetla Mihaylova Hristova-Veleva, B.S., University of Sofia  
Chair of Advisory Committee: Dr. Michael I. Biggerstaff**

The relationship between the kinematic structure of the convective line and the mesoscale storm-relative flow associated with an embedded mesovortex in the trailing stratiform region of the 28 May 1985 squall line system is examined using Doppler radar data collected during the Preliminary Regional Experiment for Stormscale Operational and Research Meteorology—Central Phase (PRE-STORM). Ten dual-Doppler analyses of the kinematic and reflectivity fields are constructed for roughly a 50-minute period over the storm's mature stage.

Reflectivity and flow fields exhibit significant variability along the convective line. Large, somewhat isolated reflectivity cores, elongated in the direction of storm propagation, were located in the southern and central portions of the storm. In contrast, the northern part of the convective line was characterized by smaller, more closely spaced reflectivity cores which were organized perpendicularly to the storm propagation vector. Deepest reflectivity cores and strongest vertical drafts were consistently found on the southern flank of the system. The southern end of the convective line expanded during the analysis period while the convective intensity of the northern end of the line continuously decreased.

A well organized cyclonic mesovortex was found at mid-level in the stratiform cloud trailing the north-central portion of the leading convective line. The variability in the structure of the convective cells along the convective line appeared to be related to the interaction between the mesoscale low-level outflow from this vortex and the environmental low-level inflow. The outflow was opposite the environmental inflow in the southern and central portions of the storm. In contrast, the outflow was directed

nearly parallel to the inflow along the northern portion of the storm system. This led to variation in the depth and direction of propagation of the convective downdraft outflow such that there was greater low-level convergence and enhanced lifting in the southern and central portions of the convective line compared to the northern part. Hence, the variability in convective structure appears to have resulted from a scale interaction between the storm-induced relative flow and the environmental winds.

## **DEDICATION**

**To my husband Omourtag and daughter Biliana for their moral support, patience and never-ending faith in me!**

**To my parents and family for bringing me up with so much love!**

## ACKNOWLEDGMENTS

I would like to express my sincere appreciation to many people for their help and suggestions without which this effort would not have succeeded.

First and foremost, I am enormously grateful to my committee chairman Dr. Michael I. Biggerstaff for his invaluable guidance and encouragement, for the many enlightening discussions and for his constructive criticism and help in focusing on the main ideas and preparing the manuscript. I wish to express my deep gratitude to Dr. James R. Scoggins for his guidance and helpful comments, for his constant support and for providing me with the opportunity to become a student member of the Cooperative Institute for Applied Meteorological Studies (CIAMS). I would also like to thank my other committee member, Dr. Juan Valdes for giving his valuable time and assistance.

I am very grateful to those persons who made other important contributions to this effort: Mr. Jerry Guynes, Mr. Michael Nelson, Mr. Daniel Austin and Mr. Christopher Lucas for their highly appreciated computer assistance; Dr. John Nielsen-Gammon for his help with Gempak graphics; Mr. Dennis Lipton, Mr. Monte Oaks, Mr. Joseph Haynes and Mr. Scott Saul for their help in unfolding the raw Doppler-velocity data and to all my fellow graduate students for their companionship and encouragement, for making me feel at home. A word of thanks goes to my office mates - Richard Igau, Capt. Stephen McMillan, Trevor Wallis, Paul Janish and Capt. William George for the many brainstorming discussions we had relating to the science of weather.

Special thanks go to Dr. Edward Zipser, Dr. Richard Orville, Prof. John Griffiths and to all CIAMS members for their support and suggestions throughout the production of this thesis.

I wish also to express my gratitude to Drs. Michael Biggerstaff and Edward Zipser for providing me with the unique opportunity to participate in the international experiment Tropical Ocean-Global Atmosphere - Coupled Ocean Atmosphere Regional Experiment (TOGA-COARE) - an invaluable experience in data collecting, which furthered my knowledge of observational and tropical meteorology.

Finally, I would like to deeply thank my husband Omourtag and daughter Biliانا for their constant support, patience and understanding, for their dedication to this effort. I am very grateful to my parents, family and friends for letting me know my work was worthwhile.

**This effort was founded by the National Science Foundation under grant ATM-9201786 and National Oceanic and Atmospheric Administration under contract NA37WA0543.**

## TABLE OF CONTENTS

	Page
ABSTRACT.....	iii
DEDICATION.....	v
ACKNOWLEDGMENTS.....	vi
TABLE OF CONTENTS.....	viii
LIST OF TABLES.....	ix
LIST OF FIGURES.....	x
CHAPTER	
I    INTRODUCTION.....	1
II   PREVIOUS STUDIES.....	3
Generation and Evolution of Mesoscale Vortices and Their Effect on the Longevity of the Convective Systems.....	3
Relationship between the Midlevel Mesovortex and the Kinematic and Reflectivity Structure of the Trailing Stratiform Area.....	5
Relationship between the Mesoscale Storm-Relative Flow and the Structure and Evolution of the Convective Area.....	7
Problem.....	10
III  DATA AND METHOD OF ANALYSIS.....	12
Instrumentation and Data.....	12
Storm Motion.....	14
Dual-Doppler Wind Analysis.....	17
IV  CASE DESCRIPTION.....	20
V   STORM MORPHOLOGY.....	39
Low Levels (surface to 1.9 km).....	43
Mid-to-Low Levels (2.4 to 3.9 km).....	58
Mid-to-Upper Levels (4.4 to 8.9 km).....	63
Upper Levels (9.4 km and above).....	68
Vertical Cross-Sections.....	72
VI  STORM EVOLUTION.....	80
Southern Flank (West Dual-Doppler Analysis Lobe).....	83
North and Central Portions of the System (East Dual-Doppler Analysis Lobe).....	93
VII CONCLUSIONS AND RECOMMENDATIONS FOR FURTHER STUDY.....	106
REFERENCES.....	111
VITA.....	115



**LIST OF TABLES**

<b>Table</b>		<b>Page</b>
1	Characteristics of the NCAR Doppler radars used during PRE-STORM..	13
2	Summary of the dual-Doppler analyses times.....	15

## LIST OF FIGURES

Figure	Page	
1	PRE-STORM radar and upper-air networks.....	
2	Composite of radar detected storm intensity at 2235 UTC on 27 May 1985.....	21
3	Cold cloud tops depicted by the infrared satellite imagery at 0030 UTC on 28 May 1985.....	22
4	As in Fig. 3 except for 0300 UTC.....	23
5	As in Fig. 2 except for 0235 UTC.....	24
6a.	As in Fig. 2 except for 0535 UTC.....	25
6b	As in Fig. 2 except for 0735 UTC.....	25
7	Low level radar reflectivity as seen from the Wichita (ICT), Kansas WSR-57 10 cm storm surveillance radar at 0910 UTC on 28 May 1985..	27
8	As in Fig. 7 except for 1150 UTC and antenna elevation of 0°.....	28
9a	Conceptual model of a horizontal cross-section through mid-level flow field and low-level reflectivity field, associated with symmetric (left) and asymmetric (right) squall line systems.....	29
9b	As in Fig. 9a except for radar reflectivity field only.....	29
10	As in Fig. 7 except for 1310 UTC and antenna elevation 0°.....	30
11	As in Fig. 3 except for 1401 UTC.....	32
12	As in Fig. 7 except for 1507 UTC.....	33
13a	As in Fig. 2 except for 1735 UTC.....	34
13b	As in Fig. 2 except for 1935 UTC.....	34
14	As in Fig. 3 except for 1801 UTC.....	35
15	Time-height cross-section of the wind field, constructed from the Monett, Missouri upper-air data.....	37
16	As in Fig. 2 except for 2135 UTC.....	38
17	Low-level (1.1°) PPI of radar reflectivity from CP4 Doppler radar at 1148 UTC on 28 May 1985 .....	41

Figure	Page
18	Conceptual model of a squall line with a trailing stratiform area viewed in a vertical cross section oriented perpendicular to the convective line (i.e., parallel to its motion).....42
19a	Streamline/isotach analysis of ground-relative winds, measured in the PRE-STORM surface mesonet network at 1150 UTC on 28 May 1985.....44
19b	Divergence field ( $\times 10^{-5} \text{ s}^{-1}$ ) measured in the PRE-STORM surface mesonet network at 1150 UTC on 28 May 1985..... 46
19c	Streamline/isotach analysis of storm-relative winds at 1150 UTC on 28 May 1985.....47
20a	1152 UTC dual Doppler analysis of kinematic and reflectivity field at 1.4 km Mean Sea Level (MSL).....49
20b	1152 UTC dual Doppler analysis of the storm-relative horizontal flow field at 1.4 km Mean Sea Level (MSL)..... 51
20c	1152 UTC dual Doppler analysis of the vertical velocity field at 1.4 km Mean Sea Level (MSL). Overlaid are the storm-relative streamlines..... 53
21	Vertical cross-section of reflectivity (upper-left panel), vertical velocity (lower-left panel), storm-relative horizontal flow in the along-line direction (upper-right panel) and storm-relative horizontal flow in the cross-line direction (lower-right panel) at 1137 UTC. The cross-section is located in the central portion of the squall line (location is marked by the X and Y coordinates of the end points, given at the two ends of the X axis) and oriented in direction, normal to the local orientation of the convective line (the horizontal axis is pointing towards $117^\circ$ from true north)..... 56
22a	As in Fig. 20a except for 3.4 km..... 59
22b	As in Fig. 20b except for 3.4 km.....60
22c	As in Fig. 20c except for 3.4 km..... 61
23	Vertical profile of the mean vertical velocity ( $\text{ms}^{-1}$ ), relative vertical vorticity ( $10^{-3}\text{s}^{-1}$ ) and divergence ( $10^{-3}\text{s}^{-1}$ ), averaged over the area of the midlevel vortex ( $-28 < X < 20$ , $59 < Y < 110$ )..... 62
24a	As in Fig. 20a except for 6.9 km..... 64
24b	As in Fig. 20b except for 6.9 km.....65
24c	As in Fig. 20c except for 6.9 km..... 66

Figure	Page
25a	Dodge City, Oklahoma (DDC) 0000 UTC 28 May 1985 skew T-log p profile of temperature, dewpoint temperature and wind..... 67
25b	As in Fig. 25a except for Oklahoma City, Oklahoma 1200 UTC..... 67
26a	As in Fig. 20a except for 11.4 km..... 69
26b	As in Fig. 20b except for 11.4 km..... 70
26c	As in Fig. 20c except for 11.4 km..... 71
27a	As in Fig. 21 except the cross-section is taken through the southern portion of the storm at 1152 UTC. The X axis is pointing toward 160° from true north..... 73
27b	As in Fig. 27a except for 1125 UTC..... 74
28	As in Fig. 21 except for 1152 UTC..... 76
29	As in Fig. 21 except for the cross-section is taken through the northern portion of the storm at 1152 UTC. The X axis is pointing toward 90° from true north..... 79
30	As in Fig. 17 except for a four panel plot presenting the reflectivity as seen by either CP3 or CP4 at four different time periods: upper-left panel - 1010 UTC low level reflectivity field as observed by the CP3 radar; lower-left panel - 1040 UTC reflectivity as seen by the CP4 radar; upper-right - 1120 UTC reflectivity as seen by CP3; and lower-right - 1148 UTC reflectivity as observed by CP4 radar..... 82
31	Dual-Doppler constructed reflectivity field of the southern flank convection at 3.4 km altitude and four time periods: upper-left panel - 1042 UTC; lower-left - 1109 UTC; upper-right - 1125 UTC; lower-right - 1152 UTC..... 85
32	As in Fig. 31 except for 6.4 km..... 86
33	As in Fig. 31 except for 5.4 km vertical velocity field..... 87
34	As in Fig. 31 except for 1.4 km flow field..... 89
35	Dual-Doppler analysis of the west lobe flow field (120 x 120 km) at 1125 UTC..... 90
36	As in Fig. 34 except for 7.9 km..... 91
37	As in Fig. 31 except for 6.9 km reflectivity field (shaded are areas with reflectivity > 25 dBz) and 7.9 km storm-relative horizontal speed field (bold contours encompass areas of wind speed > 15 ms <sup>-1</sup> )..... 92

Figure	Page	
38	Dual-Doppler constructed reflectivity field of the central and northern portions of the convective line at 3.4 km altitude and four time periods: upper-left panel - 1125 UTC; lower-left - 1137 UTC; upper-right - 1143 UTC; lower-right - 1152 UTC.....	96
39	Dual-Doppler constructed vertical velocity field of the central and northern portions of the convective line at 7.9 km altitude and four time periods: upper-left panel - 1125 UTC; lower-left - 1137 UTC; upper-right - 1143 UTC; lower-right - 1152 UTC.....	98
40	Dual-Doppler constructed storm-relative horizontal flow field of the central and northern portions of the convective line at 1.9 km altitude and four time periods: upper-left panel - 1125 UTC; lower-left - 1137 UTC; upper-right - 1143 UTC; lower-right - 1152 UTC.....	100
41a	Vertical cross-sections of reflectivity and vertical velocity fields at three time periods: 1137 UTC, 1143 UTC and 1152 UTC. The cross-sections are taken through the south-central portion of the storm system. The X axis is pointing toward 117° from true north.....	102
41b	As in Fig. 41a except for cross-line and along-line components of the storm-relative horizontal flow.....	103
42	As in Fig. 40 except for 6.4 km.....	104
43	As in Fig. 38 except for 11.4 km.....	105
44	Conceptual model of the flow field of an asymmetric squall line system with an embedded midlevel mesovortex.....	108

## CHAPTER I

### INTRODUCTION

Squall line systems, often characterized by a leading line of deep cumulonimbus with trailing stratiform precipitation, represent a significant portion of the mesoscale precipitation systems observed over the central United States (Houze et al. 1990). These storms have been observed in both the tropics (Hamilton and Archibold 1945; Zipser 1969) and midlatitudes (Newton 1950; Fujita 1955). While the general kinematic structure of squall lines is well known, the interaction of the convective region with storm-induced mesoscale circulations is still not well understood.

The latent heating and cooling that takes place within squall lines often leads to the formation of mesoscale pressure perturbations. A mid-level mesolow can form in association with lower level melting and evaporative cooling underneath latent heating in the warm, buoyant stratiform cloud deck that often trails the convective line (e.g. Biggerstaff and Houze 1991a). This pressure field and another mesolow that exists underneath sloping updrafts in the convective region (LeMone 1983) aid in the generation of rear-to-front storm-relative flow. Midlevel convergence of positive absolute vorticity into the mesolow leads to the development of cyclonic relative vorticity at mid-levels in the trailing stratiform region (Zhang and Fritsch 1987, 1988; Brandes 1990; Biggerstaff and Houze 1991b).

Occasionally, the cyclonic vorticity forms a mesoscale vortex circulation in the trailing stratiform region with storm-relative rear-inflow in the southern branch of the vortex and storm-relative front-to-rear flow in the northern branch (e.g. Houze et al. 1989; Brandes 1990). The storm-relative flow associated with these mesovortices can also affect the reflectivity structure of the squall line system by aiding in the development of an extensive stratiform precipitation region associated with the front-to-rear storm-relative flow and limiting the areal coverage of stratiform precipitation in the dry, storm-relative rear-inflow branch.

As suggested by Smull and Houze (1987) and modeled by Weisman (1992), the rear-inflow can also affect the evolution of the convective system by altering the structure of the vertical drafts in the convective region. Moreover, along-line differences

in the intensity, depth and altitude of the rear-inflow into the convective region would also be associated with the mesovortex. However, the mechanism for the interaction between the mesoscale flow and the convective line remains obscure. No observations have been presented to document the association between a stratiform region mesovortex and differences in the convective structure along the convective line.

This study addresses the question of scale interaction by examining the relation between the time and space variability of the mesovortex circulation and the time and along-line variability of the convective region in a midlatitude squall line system.

## CHAPTER II

### PREVIOUS STUDIES

To investigate the development of mesoscale circulations and their impact on the evolution and structure of the mesoscale convective systems, studies have been conducted in three major areas: (i) generation and evolution of mesoscale vortices and their effect on the longevity of the storm systems; (ii) relationship between the midlevel mesovortex and the kinematic and reflectivity structure of the stratiform area; and (iii) relationship between the mesoscale storm-relative flow and the structure and evolution of the convective area.

#### Generation and Evolution of Mesoscale Vortices and Their Effect on the Longevity of the Convective Systems

Bosart and Sanders (1981) used synoptic and rawinsonde data to investigate the structure and evolution of the mesoscale convective complex which produced the Johnstown Flood of July 1977. They found that the storm system was characterized by a pool of cool air throughout the lower troposphere and by a strong cyclonic circulation in the lower and middle troposphere, capped by an intense anticyclonic circulation in the upper troposphere. The storm system went through periodic redevelopment and persisted for more than five days, producing intensive rain over a very broad area.

Bosart and Sanders attributed the longevity of the system and its ability to reorganize to a positive feedback mechanism between the convection, the cool pool, a low level jet, and the convergence which was feeding the new convection. The mid-tropospheric mesovortex helped produce convergence which intensified the vertical velocity and helped to trigger new convection along the southern edge of the system. While this study indicated that the mesovortex could help sustain the *storm system* over a long period of time, interaction between the mesovortex and the *structure* of the convective region was not discussed.

Zhang and Fritsch (1987) performed a numerical simulation of the Mesoscale Convective Complex (MCC) that produced the 1977 Johnstown flood to examine the development of the warm-core midlevel mesovortex and its role in determining the evolution of the MCC. They found that low-level mass and moisture convergence, associated with low- to mid-level latent heat release and surface pressure falls, were



responsible for the mesovortex development. Once the horizontal dimension of the mesovortex exceeded the Rossby radius of deformation, inertial stability extended the longevity of the cyclonic circulation. The apparent interaction between the environment and the mesoscale circulation suggests that inertially stable long-lived vortices can lengthen the lifetime of a storm system by aiding in redevelopment of convection as the vortex enters a convectively favorable environment. Hence the storm system, which consists of convective and stratiform precipitation along with the induced kinematic flow fields, may go through periods of convective redevelopment even after the original zone of convection has decayed. Unfortunately, this study did not discuss the mechanism through which the downscale interaction between the mesovortex and the convective activity took place.

Zhang and Fritsch (1988) continued their investigation of warm-core midlevel mesovortices. Confirming the results of their previous work, they found that the resolvable-scale condensation was primarily responsible for generating the vortex circulation through geostrophic adjustment of the air to the pressure perturbations produced by the latent heat release at low- to mid-levels. Once again, they emphasized the importance of the vertical uniformity of the horizontal momentum which, in combination with the relatively weak environmental flow, contributed to preserving the moisture and energy. This facilitated the generation and maintenance of the warm-core structure and vortex circulation. Again, inertial stability was used to explain the longevity of the storm system. Moreover, they speculated that the longevity of the circulation made the system highly deterministic. While the study revealed the structure and evolution of the vortex and discussed the mechanism of generation and maintenance of long-lived vortices, it did not focus on the interaction between the vortex and the convective activity of the system.

Verlinde and Cotton (1990) used data collected during the Preliminary Regional Experiment for Stormscale Operational and Research Meteorology - Central Phase (PRE-STORM) to examine the structure and evolution of a mesoscale vortex couplet that developed in the Mesoscale Convective System (MCS) on 16-17 June 1985. Dual-Doppler analysis of the wind field revealed the meso- $\beta$  scale (diameter between 20-200 km) dimensions of each of the vortices. While the mechanisms for the development of rotation on the thunderstorm scale ( $d \leq 10$ -20 km) (Klemp 1987) and meso- $\alpha$  scale ( $d \geq 200$  km) (Zhang et al. 1987; Brandes 1990) are fairly well understood, the dynamics of the vortices on the meso- $\beta$  scale remains obscure. Based on the flow features and the

vorticity budget analysis, Verlinde and Cotton proposed a mechanism for the formation of the observed circulation in which vorticity generation on both meso- $\alpha$  and meso- $\gamma$  (dimensions 2-20 km) scales are present, but in a modified way. The study provided insight to understanding the development and evolution of meso- $\beta$  scale circulations. However, the question of interaction of this mesocirculation with the convection that generated it was not addressed.

Biggerstaff and Houze (1991b) studied the vertical vorticity structure of the 10-11 June 1985 PRE-STORM squall line. They found that on average, strong positive vorticity was present throughout the depth of the convective region and at mid- to low-levels in the rear of the stratiform area. At mid-levels, the two regions were separated by anticyclonic vorticity. Based on their results, a conceptual model of how the vertical vorticity structure may have developed was proposed. The initial generation of horizontal vorticity was attributed to the vertical wind shear in the along-line direction of the storm, creating horizontal "vortex tubes". The primary mechanism in developing the observed banded vorticity structure was the tilting and stretching of the vortex tubes by the mesoscale up- and downdrafts. Biggerstaff and Houze (1991b) suggested that the negative vertical vorticity inhibited the development of inertially stable circulation in midlevels and may have affected the longevity of the system. While the study, like the others mentioned above, addressed the important question of how the vertical vorticity structure affects the storm longevity, it did not discuss the interaction between the vorticity field and the original convective region.

#### **Relationship between the Midlevel Mesovortex and the Kinematic and Reflectivity Structure of the Trailing Stratiform Area**

Smull and Houze (1985) studied the radar-echo structure of the 22 May 1976 Oklahoma squall system. Wind fields were constructed based on time-space conversion of rawinsonde data. Superposition of the system relative flow and radar echo pattern suggested that the concavity, or notch, observed at the rear echo boundary of the stratiform region was produced by strong midlevel forward influx of dry air which evaporated the precipitation particles. Moreover the rear-to-front flow was associated with a midlevel cyclonic vorticity maximum identified by Ogura and Liou (1980) in their study of this case. Smull and Houze (1985) suggested that the development and forward expansion of the notch was followed by bulging and intensification of the convection downwind of the rear echo notch. However, the proposed relationship

between the midlevel cyclonic vorticity, the rear-inflow and the convection was only qualitative since dual-Doppler synthesis of the airflow at the rear was not possible due to the restricted area covered by dual-Doppler radar data.

Leary and Rappaport (1987) studied the internal structure of a squall-line system which passed through the data-collecting network of High Plains Cooperative Program (HIPLEX) on 8 June 1980. The analysis used data collected with a C-band digitized radar and an upper-air network. Superimposing the flow and reflectivity fields, they found that the cyclonic mesovortex, observed at 500 mb, was coincident with the center of curvature which the reflectivity pattern acquired during the mature stage of the system. They concluded that the curvature in the reflectivity pattern reflected an interaction between the mesoscale system-generated vortex and the fine scale substructure of the precipitation pattern. Analysis of the storm-relative flow field revealed that rear-to-front flow (RTF) corresponded to the southern portion of the midlevel mesovortex, while front-to-rear (FTR) flow predominated elsewhere. Examination of the large scale wind field showed that at midlevels there was no system relative RTF. Based on this observation, Leary and Rappaport concluded that the RTF relative winds, extending from the center of curvature of the rainbands downward toward the leading edge, were associated with the squall-line-generated mesovortex. However, the evolution of the system was not obtained, due to the steady-state assumption in their composite analysis. Thus, the question of cause and effect could not be examined.

Smull and Houze (1987b) investigated a number of squall line systems focusing on detailed examination of the rear inflow (RI). Studying the variability of the RI on the time and space scale of the system, they examined the airflow structures of three midlatitude squall lines. The flow fields of the three cases revealed the same general features: (i) in the rear of the system the strongest forward flow was observed at midlevels in association with depressed values of equivalent potential temperatures; (ii) the axis of the strongest RI then sloped downward toward the leading convective line, where it merged with the outflow from the convective-cell-downdrafts into the flow behind the gust front; and (iii) increased depth of the RI may have contributed to a decrease in the width of the stratiform area. Considering the magnitude and variability of RI in 18 different cases, Smull and Houze distinguished three different regimes of storm-relative flow at the back edge of the stratiform precipitation area: STRONG RI, WEAK RI and STAGNATION ZONE (case with little if any inflow at midlevels).

Examining the flow field of a STAGNANT-ZONE squall line, they came to the conclusion that RI developed in the stratiform region. Smull and Houze proposed that two separate processes may be responsible for the generation of the RI: (i) hydrostatic reduction of pressure under rearward sloped warm convective updrafts (LeMone 1983, LeMone et al. 1984); and (ii) the development of midlevel mesolow in the trailing stratiform region in association with latent heating above lower level melting and evaporative cooling (Brown 1979). While the study investigated many of the characteristics of the RI and hypothesized that RI plays an important feedback role in forcing the convection along the leading line, no direct evidence of the interaction between the RI and the convective region was presented.

Brandes (1990) used surface mesonetwork, rawinsonde and Doppler radar data to study the effect of the embedded midlevel mesovortex on the stratiform area of the 6 May 1985 squall line observed during PRE-STORM. Analysis of the flow field, obtained from spatially adjusted rawinsonde observations, revealed the presence of strong positive vertical vorticity in the lower to middle troposphere - levels dominated by strong rear inflow. From the analysis, Brandes concluded that the mesovortex enhanced the rear inflow which was confined to the southern part of the storm. The study emphasized the importance of the mesovortex in organizing the storm structure. However the spatial and temporal resolution of the data did not allow the mesovortex - convective scale interactions to be investigated.

#### **Relationship between the Mesoscale Storm-relative Flow and the Structure and Evolution of the Convective Area**

Chong et al. (1987) studied the kinematic structure of a tropical squall line, observed during the Convection Profonde Tropicale in 1981 (COPT81). The airflow within the system was inferred from dual- and single-Doppler radar data. One of the distinct features was the RI which was observed throughout the 0-3 km layer and extended from the stratiform to the convective region. Chong et al. computed the mass transported by the convective and mesoscale downdrafts and estimated air mass flux observed through the gust front. The mass balance revealed that the convective and mesoscale downdrafts accounted for 40% and 60%, respectively, of the rear-to-front flow behind the gust front. The results suggested that the mesoscale downdrafts play an important role in the generation of the deep cold rear-to-front flow, and therefore in the forcing of the convergence along the leading line. While Chong et al. demonstrated the

importance of scale interaction, the mechanism of the mesoscale forcing of the convective scale updrafts remained obscure and no indication on how this interaction affected the along-line variability in the convective region was provided.

Rotunno et al. (1988) used two- and three-dimensional simulations to examine the interaction between the environment and the cold pool at the leading edge of squall line systems. They suggested this interaction as the primary mechanism forcing convection. Based on the tilt of the convective updrafts, they defined three states of the system: greater-than-optimal, optimal and less-than-optimal. Furthermore, they proposed that each of these states was the result of an interaction between the positive horizontal vorticity of the vertical wind shear and the negative horizontal vorticity generated by the buoyancy gradients associated with the cold pool. While the theory (RKW) helps explain some observations, it remains an oversimplification of the actual flow field and does not address along-line variability in convective structure.

Lafore and Moncrieff (1989) used a set of 13 two-dimensional numerical simulations based on soundings from (COPT81) to study the organization and interaction of the convective and stratiform regions of tropical squall line systems. Sensitivity tests revealed that the intensity of the RI increased with the initial convective instability and was a linear function of the African Easterly Jet speed. Inclusion of ice-phase microphysics led to an increase in the strength of the RI. Enhancing the precipitation evaporation below the anvil intensified the mesoscale subsidence resulting in a less organized system. This somewhat surprising result can be explained by acknowledging that stronger subsidence will lower the rear-to-front (RTF) circulation making the RI less efficient in releasing the convective instability through convergence. Later stages of the development are characterized by lowered RI, decreased convective depth and intensity and increased slope. While acknowledging the importance of the cold pool forcing, Lafore and Moncrieff proposed the RI-enhanced convergence as another mechanism of convective forcing - an illustration of direct scale interaction emphasizing the "global" physics of the system as opposed to the "local" cold pool forcing. This study gave new insight on the structure and evolution of the system, emphasizing the importance of scale interactions for the storm dynamics. However, the study used a two-dimensional model thus excluding many of the observed cases exhibiting a profound three-dimensionality. Therefore, questions of structural and dynamic variations in the along-line direction were not addressed.

Fovell and Ogura (1989) employed a two-dimensional model to investigate the effect of the vertical wind shear on the mature phase behavior of the model-simulated storms. Sensitivity tests showed that increased vertical wind shear forced the simulated RI to intensify and at the same time affected the vertical structure of the current - the point where the current entered the cold pool from the rear moved closer to the leading edge, while the top of the system-relative inflow ascended. Thus, as the shear increased, the RI source region became elevated, therefore progressively dryer. The enhanced evaporative cooling along with the intensified RI, helped to create deeper and colder outflow. The study showed that these cold pools were associated with more vertically oriented and faster propagating storms. Thus, the rear inflow, forced to intensify by the increased shear, may have been the major mechanism for establishing the systematic balance between the vertical shear and the depth of the cold pool. While the results suggested that the RI had played an important role in organizing the model storm, the particular mechanism of interaction with the convective region still remained obscure.

Zhang and Gao (1989) used mesoscale model simulations to examine the detailed structure and evolution of the RI. Conducting different sensitivity tests they found that the generation of the midlevel and surface pressure perturbations and the related *descending* portion of the RI were a direct product of the latent-heat-induced meso-circulation. As time progressed, the RI descended forward toward the leading edge and the mesoscale downdraft tilted upshear coinciding with the descending portion of the RI. Zhang et al. (1989) described the role of the descending RI jet as a producer of convergence ahead of the system, thus aiding in the acceleration and strengthening of the leading convective activity when the system is in a convectively favorable environment, and injuring the storm otherwise. However, they did not elaborate on the mechanism of the interaction; nor did they discuss the different effects of the elevated versus descending RI on the leading convection.

Weisman (1992) extended the Rotunno et al. (1988) theory by including the horizontal vorticity inherent in the rear inflow in the horizontal vorticity balance of the cold-pool-induced and vertical-wind-shear-inherent vorticity. Varying the ambient convective available potential energy and the vertical wind shear in three-dimensional simulations, he was able to reproduce many observed RI characteristics. Based on the vertical structure of the RI, Weisman discriminated between RI remaining elevated to near the leading edge of the convection line versus RI jets descending and spreading

along the surface well behind the leading edge. Considering the different contributions of the two types of RI in the horizontal vorticity balance, Weisman concluded that the development of descending jet accentuates the upshear-tilting process, thus, weakening the system by amplifying the suboptimal state. The development of an elevated RI acted in favor of the horizontal vorticity inherent in the vertical wind shear and therefore promoted the re-establishment of an optimal state with strong upright cells along the leading edge of the cold pool. Thus, an elevated RI contributed in producing a longer-lived system. While the study gave new insights into the mechanism through which the RI influences the convection of the parent storm, it did not elaborate on the influence of the mesoscale variability of the RI properties (associated, for example, with the presence of a midlevel mesovortex) on the evolution and structure of the system.

Over the past three decades many different types of data, techniques and tools have been employed in the investigation of the MCS's structure, evolution and influence on the environment. In the early studies the air motions associated with the tropical squall lines have been inferred from the thermodynamic properties of the air flowing in and out of the systems (Hamilton and Archibold 1945; Zipser 1969, 1977; Houze 1977). Later, analysis of rawinsonde data, collected in special networks, were used to construct composite wind fields, many times using time-space conversion technique under the assumption of steady state (Ogura and Liou 1980; Gamache and Houze 1982). This type of study gave the first estimates of the mesoscale air motions. New technology (Doppler radars, wind profilers, etc.), recently employed, resolves spatial and temporal variations on the convective scale. Over the years many studies made use of two- and three-dimensional numerical simulations, which provide dynamically consistent, four-dimensional, high resolution information. Important issues on storm structure and scale interaction were addressed by performing different sensitivity tests. However, no study thus far has addressed the question of how the three-dimensional circulation associated with a midlevel mesovortex may affect the initial convective region of the storm system.

### **Problem**

One of the most exciting recent discoveries in mesometeorology, as pointed by Zhang and Fritsch (1988), is that some Mesoscale Convective Systems (MCSs) develop a mesoscale vortex within their stratiform region. During recent years many observational and numerical studies have attempted to answer different questions related

to Mesoscale Convective Vortices (MCV): (i) Are they responsible for the increased longevity of the systems which produced them? (ii) How do they affect the kinematic and reflectivity structure of the stratiform area? (iii) What is the relationship between the mesoscale storm-relative rear inflow and the structure and evolution of the convective area?

However, to date, no observational study has documented the association between a stratiform region mesovortex and differences in the convective structure along the convective line. This case study examines the flow and reflectivity structure of the 28 May 1985 squall line system addressing the following questions: (i) How did the structure and the intensity of the storm-relative horizontal flow vary along the length of the convective line? (ii) Were there associated differences in the structure and intensity of the convective cells along the convective line? (iii) Was there a relation between the space and time variability in the combined meso- and convective-scale outflow and the structure and tendencies of the convective region?



## CHAPTER III

### DATA AND METHOD OF ANALYSIS

#### Instrumentation and Data

The data used in the study were obtained during the PRE-STORM project (see Cuning 1986, for overview). The experiment took place in Oklahoma and Kansas during May and June of 1985. The observational network included four Doppler and three conventional National Weather Service (NWS) digitized radars, twelve supplemental rawinsonde sites, 14 NWS upper-air stations, 3 wind profiling systems, and a surface mesonet consisting of 84 automated stations with an average spacing of 50 km. Unfortunately, the supplemental upper-air network did not operate during the 28 May 1985 event.

The primary data for this study consists of 11 dual-Doppler analysis each covering a 120 x 120 km area of the 28 May 1985 squall line during the mature stage of the storm. The data were collected by the two 5-cm Doppler radars - (CP-3 and CP-4) operated by the National Center for Atmospheric Research (NCAR). A brief summary of the characteristics of the NCAR Doppler radars is given in Table 1. The two radars were located on a 60 km north-northwest to south-southeast baseline near Wichita, Kansas. During the period 1027 - 1200 UTC the two radars were working in a dual-Doppler scanning mode, i.e., obtaining volumes of Plan Position Indicator (PPI) scans in a synchronized fashion every 5-10 minutes. Volume scans were taken by sweeping the antenna azimuthally at a fixed elevation angle and then repeating the sweeps at several elevation angles between 0.2 and 58 deg (the elevation angle is relative to the horizontal plane through the radar location). Typically, volumes containing 25 full 360° azimuthal scans were collected every half-an-hour, with a series of three sector volume scans (over a subset of azimuths at 30 different elevation angles) collected in between. Full 360° volume scanning ensured better coverage of the entire storm, while sector scanning provided higher spatial and temporal resolution (6 min between consecutive scans).

Spatial resolution should be considered as the worst resolution among all three directions. The azimuthal resolution of multiple Doppler radar data depends on both the rotation rate of the radar and the number of samples to average for an estimation and can be expressed as:

Table 1. Characteristics of the NCAR Doppler radars used during PRE-STORM.

	Radar	
	CP-3	CP-4
Wavelength (cm)	5.45	5.49
Maximum Range (km)	135	135
Nyquist Velocity ( $\text{ms}^{-1}$ )	15.37	15.24
Peak Power (kW)	400	400
Pulse Width ( $\mu\text{s}$ )	1.0	1.0
Pulse Repetition Frequency (Hz)	1111	1111
Minimum Detectable Signal (dBm)	-113	-112
Number of Range Gates	512	512
Azimuthal Resolution (deg)	0.8	0.8
Gate Spacing (meters)	260	260
Number of Samples	64	64
Beamwidth (deg)	1.0	1.0

$$r\delta\theta = r \times (\text{Samples} / \text{PRF}) \times \text{Rate} \quad (1)$$

where  $r$  is the slant range along the radar beam,  $\delta\theta$  is the azimuthal separation (in radians) between beams, *Samples* is the number of pulses averaged together to make a single estimate of returned power, PRF is the pulse repetition frequency of the radar, and *Rate* is the rotation rate of the antenna (in radians $s^{-1}$ ). The vertical resolution is the distance between beams,  $r\delta\phi$ , where  $\delta\phi$  is the angular vertical separation between two successive PPI scans. Scanning strategy adopted during PRE-STORM (rotation rate of  $13.3^{\circ}s^{-1}$  for sector scans and  $14.8^{\circ}s^{-1}$  for the full  $360^{\circ}$  scans) yields azimuthal resolution no worse than 0.9 km within a 60 km slant range. Vertical resolution below 8 km is also no worse than 1 km. Thus, the inherent spatial resolution of the Doppler radar data used in this study is no worse than 1 km within 60 km slant range.

Nearly continuous scanning between 1033 UTC and 1148 UTC provided five sector scans and three  $360^{\circ}$  scans from each radar (Table 2). All of these data have been analyzed as part of this study. 1308 UTC dual-Doppler analysis performed by Houze et al. (1989) was also included.

To investigate the impact of the environmental variability on the along-line variance in the convective structure, the data from the surface mesonet were studied. Each of the 84 stations recorded 5-minute averages of pressure, temperature, moisture, and wind measurements, and 5-minute totals of the rainfall. For each station, these data were plotted in a time series to check for missing or suspect data which were removed from the data set if found.

### Storm Motion

Subjective time series analysis of the surface mesonet data revealed the wind shift associated with the gust front propagation through the PRE-STORM area (Fig. 1). These isochrones of wind-shift were used to define the storm motion. For consistency with previous studies (e.g. Garnache and Houze 1982, 1985; Biggerstaff and Houze 1991a) the storm motion is defined as the propagation vector of the bowed out central portion of the gust front. It was determined to be from west-northwest ( $295^{\circ}$ ) at  $20 \text{ ms}^{-1}$ . All dual-Doppler derived winds shown here are relative to the storm motion.

Table 2. Summary of the dual-Doppler analyses times.

Radar	Start Time (UTC)	Stop Time (UTC)	Min/Max Azimuth (deg)	Min/Max Elevation (deg)	Doppler Analysis Time (UTC)	Doppler Lobes
CP-3 CP-4	10:33:28 10:33:47	10:38:17 10:39:35	195 - 350 207 - 360	0.2 - 40.4 0.2 - 58.0	10:36:32	West
CP-3 CP-4	10:40:00 10:40:09	10:50:12 10:45:04	000 - 360 000 - 360	0.2 - 58.0 0.2 - 13.4	10:42:36	East/West
CP-3 CP-4	11:06:50 11:06:57	11:12:33 11:12:45	182 - 338 226 - 022	0.2 - 58.0 0.2 - 58.0	11:09:48	West
CP-3 CP-4	11:12:38 11:12:53	11:18:21 11:18:42	185 - 338 226 - 022	0.2 - 58.0 0.2 - 58.0	11:15:40	West
CP-3 CP-4	11:20:00 11:19:59	11:30:09 11:30:32	000 - 360 000 - 360	0.2 - 58.0 0.2 - 58.0	11:25:05	East/West
CP-3 CP-4	11:34:30 11:34:30	11:40:15 11:40:24	357 - 150 335 - 128	0.2 - 58.0 0.2 - 58.0	11:37:27	East
CP-3 CP-4	11:40:20 11:41:52	11:46:04 11:47:04	354 - 150 335 - 128	0.2 - 58.0 0.2 - 44.3	11:43:42	East
CP-3 CP-4	11:48:00 11:47:40	11:58:08 11:57:58	000 - 360 000 - 360	0.2 - 58.0 0.2 - 58.0	11:52:54	East/West
CP-3 CP-4					13:08:	East

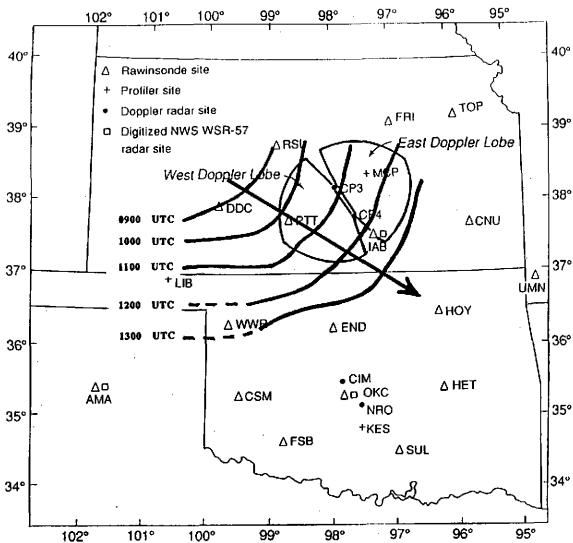


Figure 1. PRE-STORM radar and upper-air networks. Also plotted are the isochrones of the gust front associated with the 28 May 1985 squall line system. Gust front position was determined based on time-series analysis of the data from the PRE-STORM surface mesonetwork.

### Dual-Doppler Wind Analysis

A separate dual-Doppler analysis was performed on each of the lobes of Doppler radar data collected at times in Table 2. The technique of Biggerstaff and Houze (1991a) was used.

Before initiating the analysis, Doppler data from each of the radars were carefully edited using the RDSS (Research Data Support System) software (Oye and Carbone 1981). Editing included velocity unfolding, removing of the noise in the velocity field by thresholding out points with returned power less than -110 dBm and, finally, removing areas of suspected second trip echoes.

Next, the reflectivity and unfolded radial velocity from each of the radars were interpolated from their polar coordinate systems into a common Cartesian grid with dimensions 120 x 120 x 15.4 km with a 1 km horizontal grid spacing and 0.5 km vertical spacing. The interpolation was accomplished using the bilinear interpolation method within SPRINT (Sorted Position Radar Interpolation) software (Mohr et al. 1979). The bilinear scheme is designed to better preserve small variations in the observations (Mohr and Vaughan 1979) as compared to the Cressman interpolation. Radar reflectivity was converted from a logarithmic scale to a linear scale prior to the interpolation.

Dual-Doppler syntheses were then performed, using CEDRIC (Cartesian Editing and Display of Radar Data under Interactive Control) software (Mohr and Miller 1983). To account for the horizontal translation of the storm during the 6-10 minute scan time, each data point was adjusted horizontally based on the storm motion and the time between the data collected at that point and the mean time of the volume scan.

Knowing the radial velocity fields from both radars and the radar geometry, initial estimates of the horizontal wind components were obtained, under the assumption of zero vertical velocity. Values at grid points with bad dual-Doppler geometry (for example along the baseline) were then removed by thresholding out those points for which either USTD or VSTD (geometric terms relating the variance in the  $u$  and  $v$  components to the variance in the radial velocity measurements) exceeded the value of 5.5. Since patching acts like a filter, this procedure was performed before patching the  $u$  and  $v$  components to minimize the effect of the bad velocity estimates on the rest of the data set.

Fallspeeds were removed using a fallspeed-reflectivity relationship. For this, the maximum radar reflectivity fields from both radars were used at each grid point.

Following Marks and Houze (1987), particle fallspeed was calculated based on the reflectivity - fallspeed relationship:

$$V = (\rho_0/\rho)^{0.4} a Z_e^b \quad (2)$$

where  $a = 2.6$        $b = 0.107$       for water

$a = 0.817$        $b = 0.063$       for ice

where  $\rho$  is air density and  $\rho_0$  is the surface-level air density.

The effective radar reflectivity factor  $Z_e$  in standard units ( $\text{mm}^6 \text{m}^{-3}$ ) was computed from the combined reflectivity field. Particle fallspeeds were calculated in units  $\text{ms}^{-1}$ . Density was assumed to have an exponential profile with a scale height of 10 km. Particles were assumed to be water below 2.9 km and ice above that level. A mixed layer of water and ice was assumed at 2.9 km and the particle fallspeed was computed as the average of the two. These fallspeeds were then used along with the first estimate of the u and v components to compute a second estimate of the horizontal wind.

Next, the horizontal wind field was patched to fill any well bounded small holes. Then a filter was applied to remove the short waves not resolved by the data. As already discussed, radar data resolution within a 60 km range was on the order of 1 km. According to Carbone et al. (1985) five independent samples within one wavelength ensure 75% recovery of the wave amplitude (i.e. energy) and a comparable accuracy of the phase distortions (expressed in terms of spatial displacement from the actual position of sinusoidal nodes and peaks). Their study suggests that the energy and phase of a particular wavelength would be well resolved with six to eight independent measurements per wavelength. According to this, the 1 km resolution of the used data set determines the minimum resolvable wavelength to be on the order of 6 km. To filter out the smaller scale phenomena, a two-step Leise (scale-telescoped) filter (Leise 1981) was used. The frequency response for this filter indicates that 60% (80%) of the energy associated with 7 km (8 km) wavelength is retained. Wavelengths of 5 km and less are almost totally cut off (less than 10% of the energy is retained).

Patched and filtered horizontal wind components were used to compute the horizontal divergence field. Divergence was then patched and decimated at grid points where either u or v wind components did not originally exist. This was necessary to ensure good vertical continuity along the edges of the data. To obtain the vertical velocity field the anelastic continuity equation

$$\rho \delta u/\delta x + \rho \delta v/\delta y + \delta(\rho w)/\delta z = 0 \quad (3)$$

was integrated downward from the echo top. Density was assumed to decay exponentially with height. The upper boundary condition for the vertical velocity field was defined as  $0.25 \text{ ms}^{-1}$  at grid points where reflectivity exceeded 18 dBz and zero otherwise. Selection of this boundary condition reflects the idea that high reflectivity cores aloft are associated with enhanced upward motion at upper levels (Biggerstaff and Houze 1991a). The obtained vertical velocity field was decimated at grid columns where the downward integration began below 8 km, considering these levels to be too far from the upper boundary for the boundary condition to be valid. The thresholded vertical velocity field was then patched and used with the original estimates of the  $u$  and  $v$  components (the one corrected for the particle fallspeed only) to compute the new estimates of the horizontal wind field.

The described procedure was repeated until the absolute value of the difference between two consecutive estimates of the horizontal wind components became on the mean less than  $0.1 \text{ ms}^{-1}$  at each level. Generally four to five iterations were required for the horizontal wind components to converge. The last  $u$  and  $v$  estimate was then patched and filtered and vertical velocity was computed from the convergence field in order to ensure mass continuity between all three wind components.



## CHAPTER IV

### CASE DESCRIPTION

The storm system which moved through the PRE-STORM data collecting network on 28 May 1985 originated from isolated thunderstorms first observed along the Nebraska-Wyoming border at about 1930 UTC on the 27th. The convection activity intensified and by 2230 UTC the southernmost thunderstorm had developed a hook echo and Bounded Weak Echo Region (BWER), characteristic of a severe tornadic storm (Fig. 2)\*. Infrared satellite imagery at 0030 UTC (Fig. 3) revealed another severe weather signature. There was a cold "V"-shape in the anvil top with marked downstream warming from the center of the V. McCann (1981) noted this satellite signature was associated with significantly deep overshooting cloud tops in severe thunderstorms. The storm system continued to intensify and propagate to the ESE. Augustine et al. (1988) noted that the anvil top of this storm system first satisfied the modified MCC criteria (Maddox 1980) at 0300 UTC on 28 May (Fig. 4). The 0235 UTC radar summary (Fig. 5) reveals the supercellular character of the convection underneath this broad circular cloud shield.

The convective organization changed rapidly between 0535 UTC (Fig. 6a) and 0735 UTC (Fig. 6b). By 0735 UTC, the supercellular characteristic had given way to a more multicellular character with an east-northeast to west-southwest orientation. The most intense convective cells, with cloud tops exceeding 16 km, were located in the southwest end of the line and may have retained some of its supercellular character. During the previous six hours radar observed hail had been continuously reported in association with this portion of the storm. Moreover, a severe weather watch had been placed into effect for the same area from 0530 to 0830 UTC. More uniform, weaker intensity echoes were found trailing the convective line to the northwest. Infrared satellite imagery (not shown) indicates that a single neatly-circular upper-level cloud shield extended over the entire convective system.

The squall line system passed through the PRE-STORM meso-network roughly between 0800 and 1500 UTC on 28 May. Low-level radar reflectivity from the Wichita WSR57 radar indicates that the structure of the storm changed significantly during this

---

\* Legibility of the text on this and the other Radar Summary figures is not important.

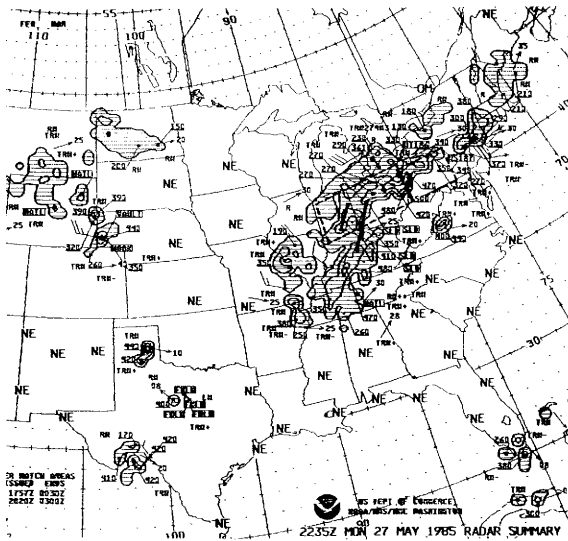


Figure 2. Composite of radar detected storm intensity at 2235 UTC on 27 May 1985. Contoured are intensity levels 1, 3 and 5 representing, respectively weak, strong, and intense echoes. Wind barbs indicate area or line propagation vector (speed is in knots). Bold lines mark solid lines of echoes. Underscored numbers represent echo tops in hundreds of feet. Dashed boxes mark weather watch areas, declared by the NWS. HOOK indicates probable tornado and VAULT marks Bounded Weak Echo Region (BWER) - radar signature indicating very strong updrafts, likely related to severe weather.

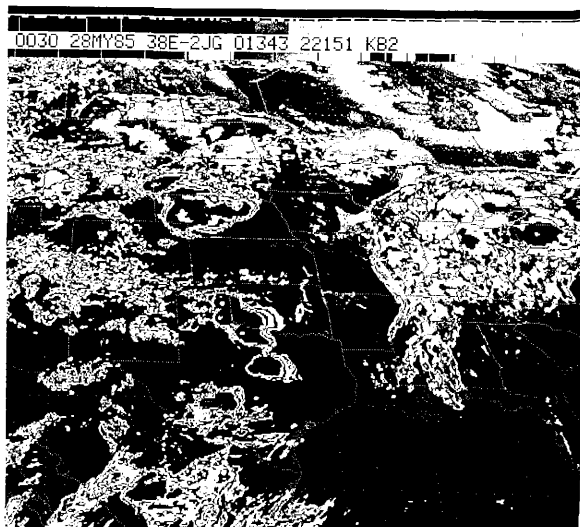


Figure 3. Cold cloud tops depicted by the infrared satellite imagery at 0030 UTC on 28 May 1985. Alternating white/black pattern denotes successively colder cloud tops.

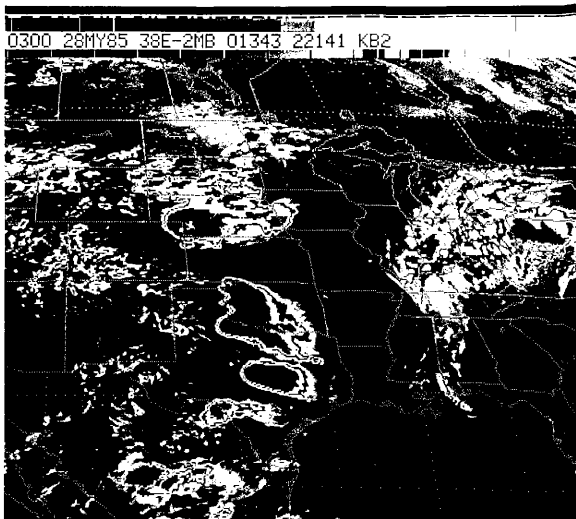


Figure 4. As in Fig. 3 except for 0300 UTC.

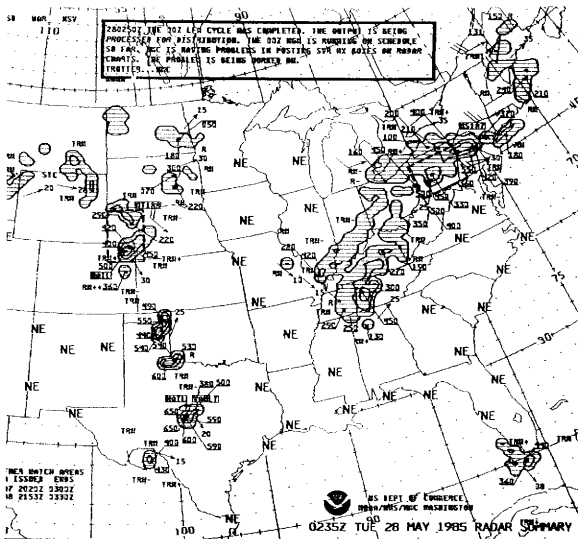


Figure 5. As in Fig. 2 except for 0235 UTC.

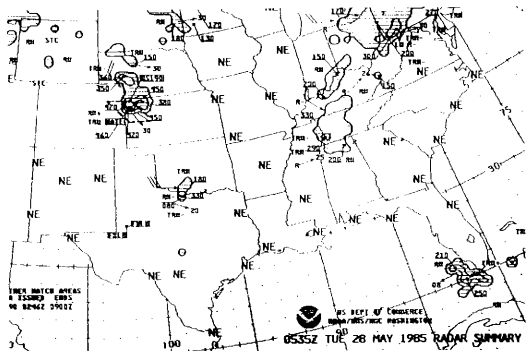


Figure 6a. As in Fig. 2 except for 0535 UTC.

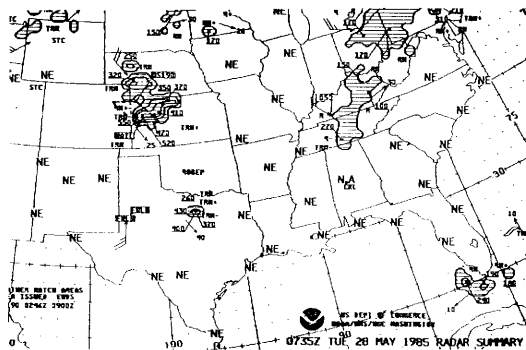


Figure 6b. As in Fig. 2 except for 0735 UTC.

period. Activity in the southern end of the storm weakened considerably after 0735 UTC. By 0910 UTC the convection was organized in a quasi-two-dimensional continuous line of intense reflectivity extending for about 180 km in a northeast-southwest direction (Fig. 7). Stratiform precipitation trailed the convective line to the northwest. The stratiform region expanded to the north and northwest after 0910 UTC and the southern flank of the convective region also expanded. However, along the southern end of the storm system there was little stratiform precipitation, as inferred from the radar reflectivity (Fig. 8). Hence, after 0910 UTC the stratiform region became asymmetric, with most of the echo confined to the northern half of the storm system.

It is believed that this asymmetry in the distribution of stratiform precipitation was associated with both the rapid expansion of the southern end of the convective line and the development of a midlevel cyclonic circulation which may have acted to evaporate hydrometeors in the southern, rear-inflow, branch of the circulation. Thus, the cyclonic circulation appears to have been well formed by 1150 UTC on 28 May. The storm system noted at 1150 UTC exhibits many of the features characteristic of an asymmetric squall line system as captured in the conceptual model of Houze et al. (1989; 1990) (Fig. 9a and Fig. 9b). First, the distribution of stratiform rain was highly asymmetric and was located behind the north-central portion of the leading convective line. Secondly, both the observed and conceptual storm systems tend to bow out in the south-central portion of the line (Fig. 9a). Finally, there is significant variability in the structure of the convective cells along the line with more isolated cells located on the southern flank of the system and generally weaker cells along the northern end of the convective line (Fig. 9b). The strong correlation between the 28 May 1985 storm system and the conceptual model of an asymmetric squall line system suggests that the 28 May storm may be extremely representative of this class of convective system. Hence, the results of this study should extend well beyond our single case analysis.

During the next hour the system continued to expand in length, becoming even more asymmetric, as the stratiform cloud progressively dissipated in the southern portion of the system (Fig. 10). However, the isolated reflectivity cores observed earlier were no longer evident. Instead, the convection was organized in an almost continuous line of intense reflectivity with the strongest cores located in the bowed out south-central portion of the line. Close examination of the reflectivity data between 1150 and 1310 UTC suggests that the new organization developed as a result of two processes: southward expansion of the convection, and merging between the isolated south-central

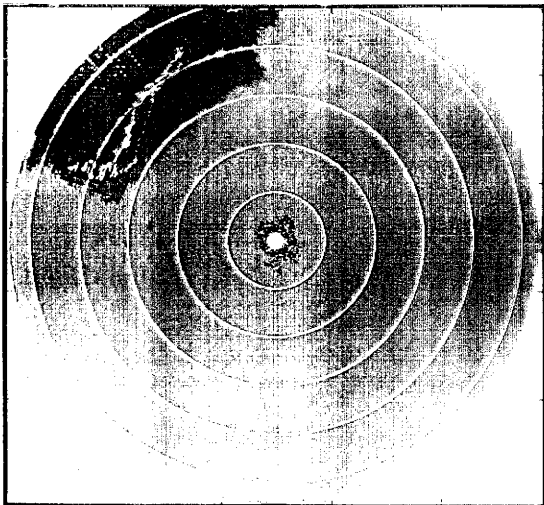


Figure 7. Low level radar reflectivity as seen from the Wichita (ICT), Kansas WSR-57 10 cm storm surveillance radar at 0910 UTC on 28 May 1985. Antenna elevation is  $1.3^{\circ}$ . Range rings are every 50 km. Shading corresponds to radar reflectivity as follows: light gray -  $< 0$  dBz; dark gray - from 1 to 14 dBz; black - from 15 to 24 dBz; white - from 25 to 29 dBz; repeat black -  $> 30$  dBz.



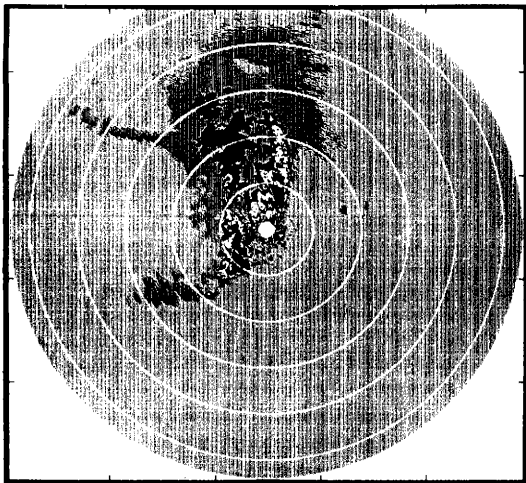


Figure 8. As in Fig. 7 except for 1150 UTC and antenna elevation of  $0^\circ$ .

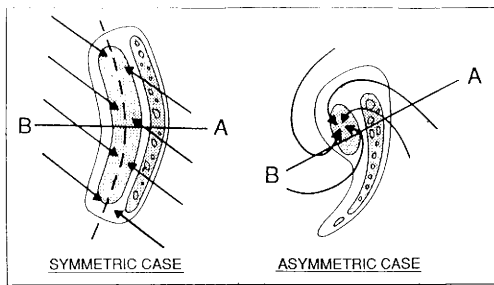


Figure 9a. Conceptual model of a horizontal cross-section through mid-level flow field and low-level reflectivity field, associated with symmetric (left) and asymmetric (right) squall line systems. Shading indicates regions of higher reflectivity. From Houze et al. (1989).

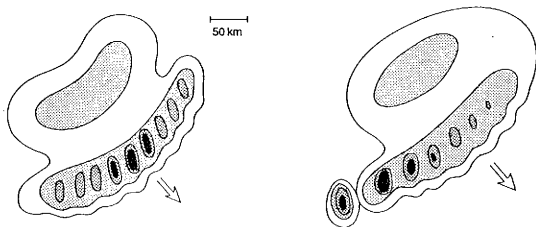


Figure 9b. As in Fig. 9a except for radar reflectivity field only. Large vector indicates direction of system motion. Levels of shading denote increasing radar reflectivity, with most intense values corresponding to convective cell cores. Horizontal scale and north arrow are shown. From Houze et al. (1990).



Figure 10. As in Fig. 7 except for 1310 UTC and antenna elevation 0°.

cells. The previously observed tendency for weaker convection along the northern portion of the line was even more pronounced at the latter time.

Dual-Doppler analysis of the flow field at 1308 UTC, performed by Houze et al. (1989), revealed the presence of a well-defined mesovortex (horizontal dimensions on the order of 100 km) located in the stratiform area (about 100 km due north of the radar site). This vortex signature is clearly observed in the reflectivity field indicated in Fig. 10. There is enhanced stratiform precipitation in the FTR branch of the circulation associated with the continuous backward transport of ice particles and cloud drops expelled from the convective region. To the south, the RI branch entrained dry, midlevel, low equivalent potential temperature air which produced significant evaporation and lead to the observed reflectivity notch (75 km due north from the radar site). By 1401 UTC, the satellite IR pattern suggests a strong anticyclonic upper-level outflow above the midlevel cyclonic mesovortex (Fig. 11). The Wichita radar indicates that important changes in the structure of the convective line have also taken place during the past hour.

Three important tendencies were noted in the evolution of the reflectivity structure during the period between 1310 and 1510 UTC. First, the preferred location of the most intense reflectivity cores was consistently on the southern flank of the convective line. Secondly, the continuous strong convection along the south-central portion of the line was associated with extension of the stratiform cloud further to the south, behind the central portion of the storm. Lastly, the central portion of the storm continued to bow forward and exhibited a significant displacement relative to the remainder of the line at 1507 UTC (Fig. 12).

By 1507 UTC, the squall line had already propagated past the denser portion of the PRE-STORM network. National radar summaries and satellite data indicate that the storm system continued propagating to the east-southeast. At 1730 UTC the system entered northwestern Arkansas. It appears that the storm system intensified between 1735 and 1935 UTC (Fig. 13). A severe weather watch was issued for the region covered by the southern flank where echo tops exceeded 15 km. Progressive drying out in the stratiform cloud behind this portion of the storm was apparent in the 1801 UTC satellite IR data which showed a significant notch at the rear of the southern portion of the cloud shield (Fig. 14). By 2000 UTC the leading line of convection passed through Little Rock, Arkansas while the stratiform area extended north-northwestward into central Missouri. Wind fields from upper-air soundings taken at Monett, Missouri

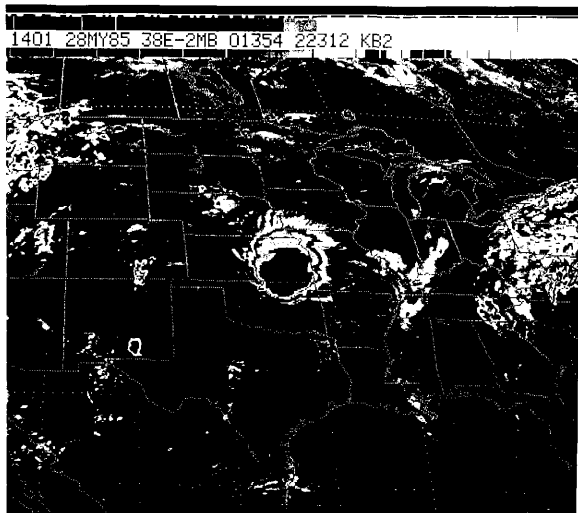


Figure 11. As in Fig. 3 except for 1401 UTC.

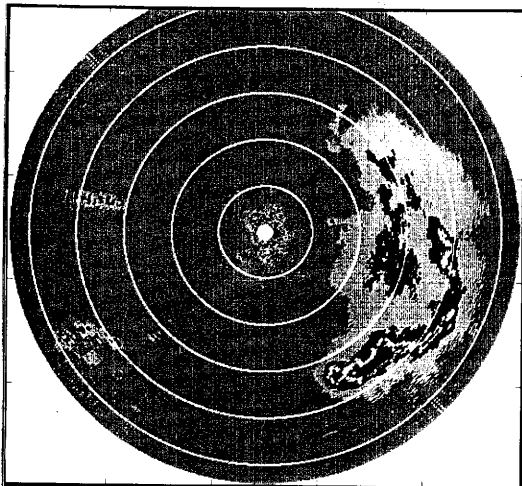


Figure 12. As in Fig. 7 except for 1507 UTC. Shading indicates radar reflectivity as follows: dark gray - < 0 dBz; light gray - from 1 to 14 dBz; black - from 15 to 24 dBz; white - from 25 to 29 dBz; repeat black - > 30 dBz.

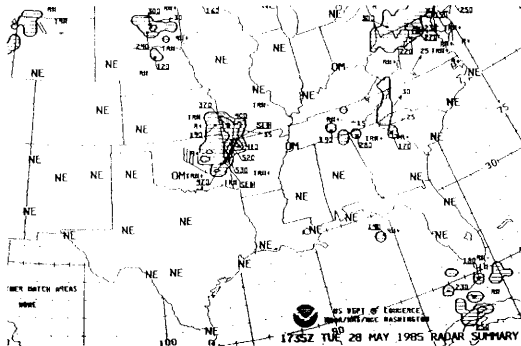


Figure 13a. As in Fig. 2 except for 1735 UTC.

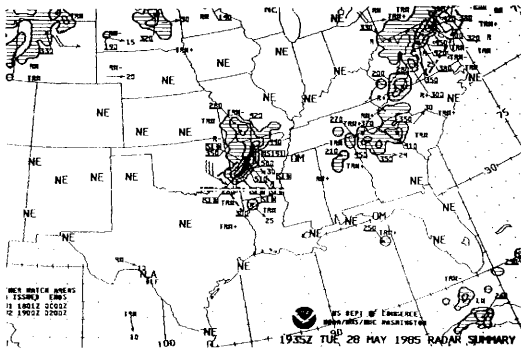


Figure 13b. As in Fig. 2 except for 1935 UTC.

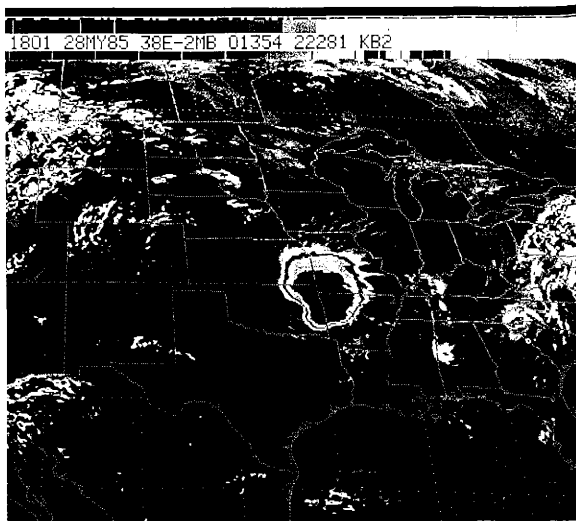


Figure 14. As in Fig. 3 except for 1801 UTC.



(UMN) show a storm-relative non-environmental RTF flow at levels between 4 and 6 km (Fig. 15). This suggests that the mesoscale cyclonic circulation was still intact and passed to the north of UMN before 0000 UTC on 29 May. The radar summary at 2135 UTC (Fig. 16) further illustrates the pronounced curvature of the leading line of convection and the asymmetric distribution of stratiform precipitation, assumed to be depicted by the intensity level 1.

The storm system continued moving through the southeast portion of the United States but began to dissipate. By 0130 UTC on 29 May the anvil cloud no longer met the MCC criteria (Augustine et al. 1988). By 0535 UTC on 29 May only stratiform precipitation was evident in the national radar summary.

The system, which first originated on the Nebraska-Wyoming border, lived for about 35 hours and propagated more than 1600 km before it dissipated along the Mississippi-Alabama border at about 06 UTC on 29 May. It produced an extensive cloud shield which satisfied the modified MCC criteria for a period of 30 hours and was found to be the longest lived MCC observed during PRE-STORM (Augustine et al. 1988). The well-organized mesoscale midlevel cyclonic vortex, observed in the stratiform area of this highly asymmetric squall line system, was likely instrumental in prolonging the life of the system.

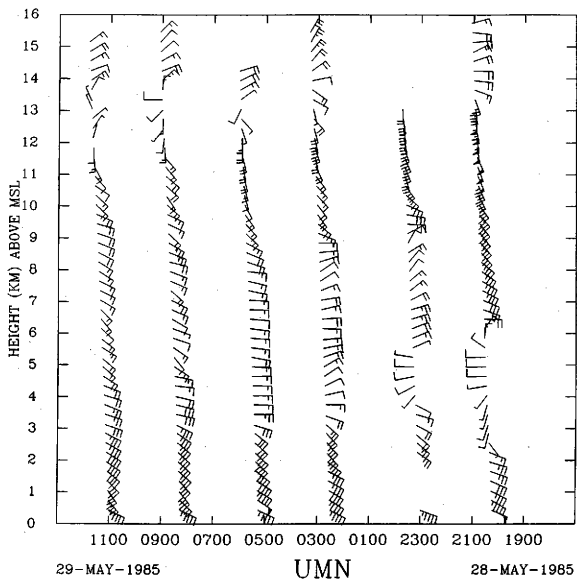


Figure 15. Time-height cross-section of the wind field, constructed from the Monett, Missouri upper-air data. Time (UTC) increases from right to left. Plotted are storm-relative winds (in knots). Assumed storm motion is from  $295^{\circ}$  at  $20 \text{ m s}^{-1}$ .

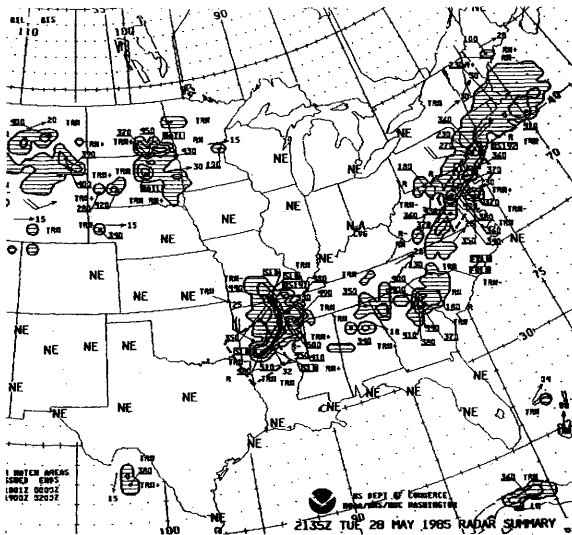


Figure 16. As in Fig. 2 except for 2135 UTC.

## CHAPTER V

### STORM MORPHOLOGY

The squall line system propagated through the CP3 and CP4 dual-Doppler area between 10 and 14 UTC on 28 May. To ensure higher time resolution, the sector-scanning strategy was adopted with attention being contiguously focused on different segments of the system as it passed through. As a result, the south and north portions of the line were observed at slightly different time periods. Fortunately, the 1125 and 1152 UTC volume scans covered both portions of the storm. From these data we can determine the along-line variability without having to be concerned about temporal variations affecting our interpretation.

Since the storm system evolved as it transversed the Doppler network, the kinematic and precipitation structure will first be described using a single analysis period, 1152 UTC. After carefully documenting the mature-stage structure of the storm system, the evolution of the squall line as it propagated through the Doppler network will be presented. Note that at 1152 UTC the southernmost flank of the convective line had already passed out of the dual-Doppler analysis domain. Therefore it is not possible to elaborate on the kinematic structure of this part of the storm. However, the reflectivity and flow features of this region will be presented in the next chapter where the evolution of the system's southern portion is described.

The low-level reflectivity field (Fig. 17) is characterized by an extensive stratiform precipitation region trailing the northern and north-central portions of the convective line. The absence of stratiform precipitation behind the southern flank convection classifies the squall line system as asymmetric (Fig. 9a and Fig. 9b). The broad region of stratiform precipitation is separated from the leading convection by a well defined reflectivity minimum, or transition zone (Biggerstaff and Houze 1993). This organization is common for many leading-line trailing-stratiform squall line systems (Houze et al. 1989). Indeed, a two-dimensional vertical cross-section perpendicular to the orientation of the convective line is often used as a conceptual model for this class of storm system (Fig. 18). However, the structure of this convective line was not strictly two-dimensional. The central portion of the line was characterized by strong, large, somewhat isolated reflectivity cells, which were elongated in the direction of storm propagation. The northern flank of the storm was dominated by smaller, closely spaced,

Figure 17. Low-level (1.1°) PPI of radar reflectivity from CP4 Doppler radar at 1148 UTC on 28 May 1985 . Maximum range of the circular display is 135 km.



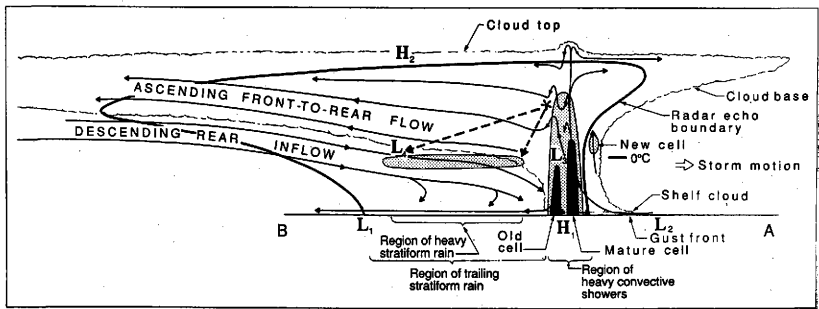


Figure 18. Conceptual model of a squall line with a trailing stratiform area viewed in a vertical cross section oriented perpendicular to the convective line (i.e., parallel to its motion). From Houze et al. (1989).

weaker reflectivity cores which were organized in a line perpendicular to storm propagation. The southern flank of the convective line was rapidly developing at this time. This region developed characteristics more typical of the central portion of the storm than the northern portion. This along-line variability in the reflectivity structure can not be represented in the two-dimensional conceptual model of squall line systems. Yet, the low-level reflectivity structure presented in the plan view conceptual model (Fig. 9b) indicates that this along-line variability may be fundamental mode of organization in asymmetric squall line systems. It is likely that the basic flow patterns observed in this case will also be generally representative of other asymmetric squall lines.

The description of the air flow patterns is first subdivided by height intervals and presented in horizontal cross-sections to depict the full three-dimensional variability of the storm system. Representative vertical cross-sections taken perpendicular to the convective line orientation over different parts of the storm will be used at the end to summarize the vertical structure and along-line variability. In the lowest layer (surface to 1.9 km), the convergence between the meso- and convective-scale outflow and the environmental inflow is well documented. Between 1.9 and 3.9 km the cyclonic circulation associated with the mesovortex is best illustrated. The rear-inflow portion of the mesovortex circulation is evident up through 8.4 km. Above 8.4 km, only the strong divergent front-to-rear flow was observed.

#### **Low Levels (surface to 1.9 km)**

The surface flow at 1150 UTC as illustrated by the ground-relative streamline/isotach analysis from surface mesonet data (Fig. 19a) shows the sharp line of confluence between the mesoscale and convective-scale outflows and the environmental inflow. Interestingly, the curvature of the convective line corresponds to the orientation that maximizes the low-level convergence at the front of the storm system. The almost north-south orientation of the northern portion of the system is almost perpendicular to the easterly inflow in that part of the environment (southeast Kansas). The central portion of the convective line is also oriented to nearly perpendicular to the low-level inflow, as the environmental winds in northcentral Oklahoma are from the southeast. The east-west orientation of the southern flank of the convective line is almost perpendicular to the southerly low-level inflow in that part of the environment (northwest Oklahoma). Hence, the orientation of the convective line seems to be strongly related to the interaction between the outflow from the storm



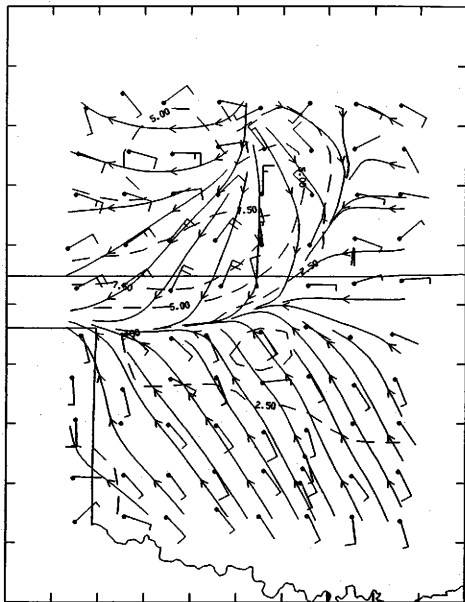


Figure 19a. Streamline/isotach analysis of ground-relative winds, measured in the PRE-STORM surface mesonet network at 1150 UTC on 28 May 1985. Dimensions of the domain are 500 x 650 km. Wind speed is contoured every  $2.5 \text{ ms}^{-1}$  (dashed lines).

system and the environmental inflow at low levels. Despite the correspondence between the squall line curvature and the direction of environmental inflow, the strongest convergence was located along the southern and central portions of the system (Fig. 19b). The ground-relative flow (Fig. 19a) suggests that the main reason for this asymmetry (with respect to the leading line) was the preferred southward expansion of the divergent outflow. (Note that the region of maximum divergence was in the northern portion of the storm system in association with the heaviest stratiform precipitation). In a recent modeling study, Skamarock et al. (1993) found that the Coriolis force acted to deflect the mesoscale outflow to the right of its direction of propagation, thus aiding the southward enhancement of the outflow winds.

For consistency with the storm-relative dual-Doppler derived winds discussed hereafter, the storm-relative surface flow is also shown (Fig. 19c). However, subtracting the considerably high storm speed ( $20.5 \text{ ms}^{-1}$ ) from the rather weak environmental flow masks the spatial variability of the surface winds, thus practically hiding the convergence line marked in the ground-relative flow. The poor representation of the surface convergence line at this time is probably also due to the insufficient spatial resolution of the surface mesonetwork (the distance between the stations is on the order of 50 km).

Dual-Doppler analysis of the radar data reveals the highly three-dimensional structure of the flow above the surface in regions where sufficient precipitation particles were present to return signal above the noise level of the radar receiver (Fig. 20 a-c). The center of divergence appears to be located in the northern portion of the storm system in an area of mesoscale descent, associated with the most intense stratiform precipitation (Fig. 20 a-c). Based on this, the low level outflow, located well behind the leading convection, is associated with the mesoscale downdraft instead of convective downdraft. Note the presence of two distinct flow regimes, found on either side of the divergence line. The cyclonic curvature of the flow in the northern portion of the system is directed nearly parallel to the inflow observed just ahead of the strong reflectivity cores (Fig. 20a). Hence, the mesoscale outflow does not contribute significantly to the convergence along the leading edge of the northern portion of the squall line system. In contrast, the anticyclonically curved mesoscale outflow in the central portion of the storm is directed nearly opposite the low-level inflow along the central portion of the squall line. Here the mesoscale outflow adds a significant component to the low-level convergence. Indeed, the orientation of the reflectivity cores is along the direction of the

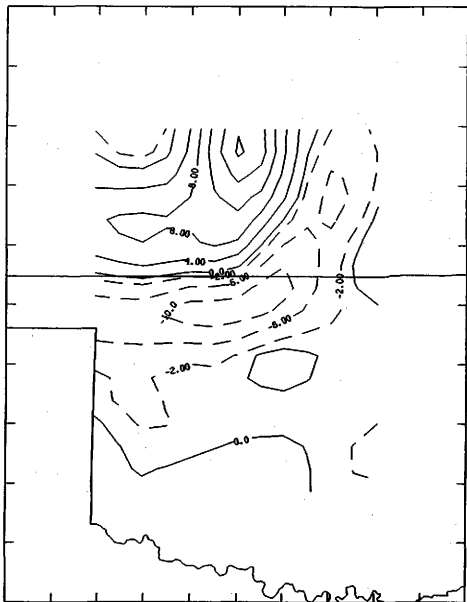


Figure 19b. Divergence field ( $\times 10^{-5} \text{ s}^{-1}$ ) measured in the PRE-STORM surface mesonet network at 1150 UTC on 28 May 1985. Dimensions of the domain are 500 x 650 km. Divergence field is contoured every  $4 \times 10^{-5} \text{ s}^{-1}$  with solid (dashed) lines indicating positive (negative) values.

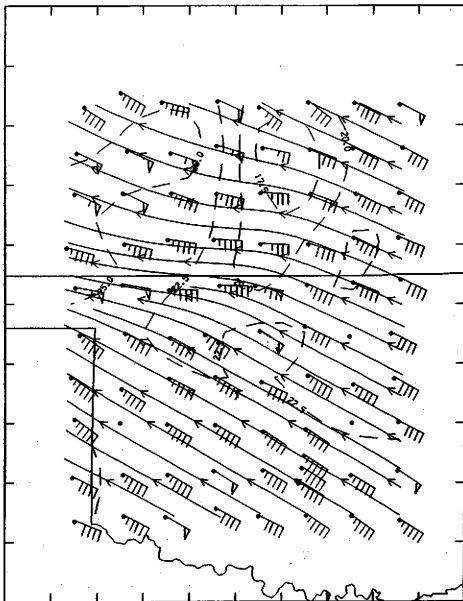


Figure 19c. Streamline/isotach analysis of storm-relative winds at 1150 UTC on 28 May 1985. Storm motion of  $20 \text{ ms}^{-1}$  from  $297^\circ$  is subtracted from the ground-relative winds measured in the PRE-STORM surface mesonet. Dimensions of the domain are  $500 \times 650 \text{ km}$ . Wind speed is contoured every  $2.5 \text{ ms}^{-1}$  (dashed lines).

Figure 20a. 1152 UTC dual Doppler analysis of kinematic and reflectivity field at 1.4 km Mean Sea Level (MSL). Reflectivity field is contoured every 5 dBz starting at 5 dBz. Areas with reflectivity in excess of 25 dBz are shaded. Overlaid are the storm-relative streamlines. Plotted area is 200 x 160 km with 1 km grid spacing. The origin of the grid is collocated with the CP4 radar.

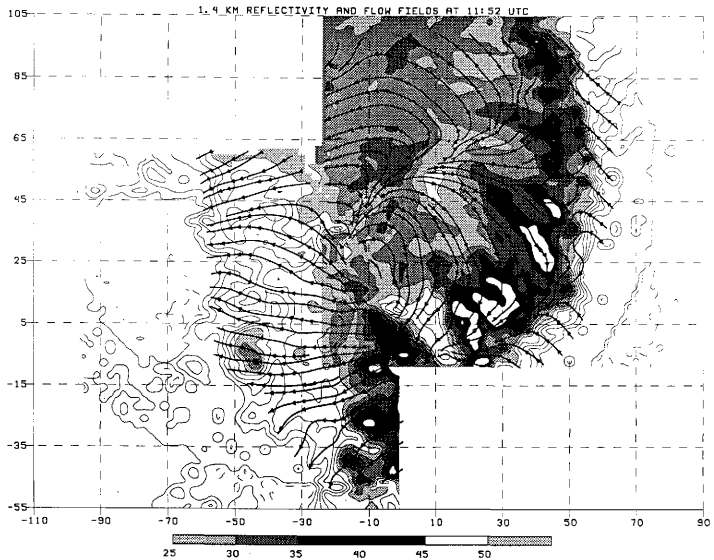
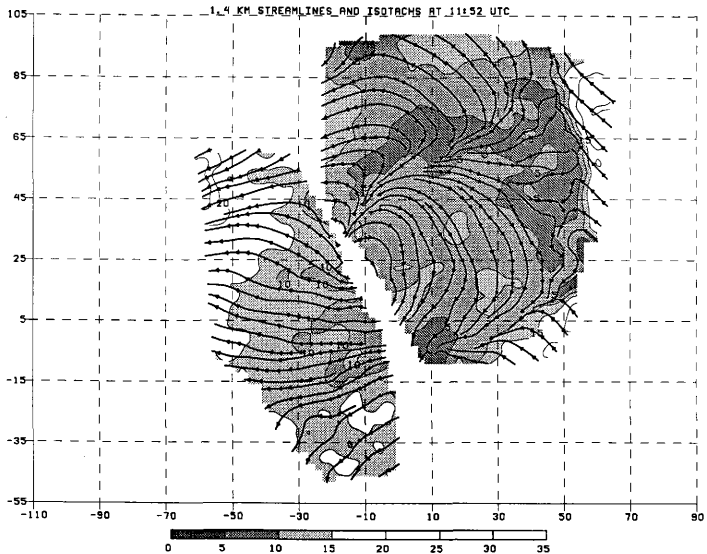
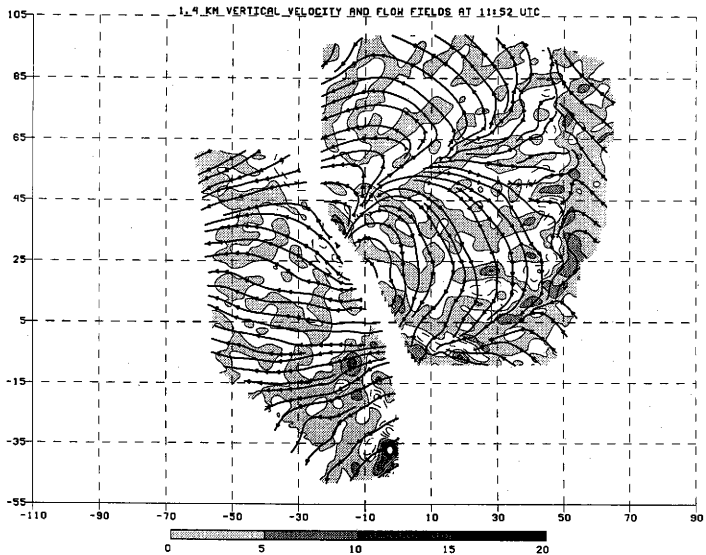


Figure 20b. 1152 UTC dual Doppler analysis of the storm-relative horizontal flow field at 1.4 km Mean Sea Level (MSL). Wind speed is contoured every  $5 \text{ ms}^{-1}$ . Areas with wind speed  $< 15 \text{ ms}^{-1}$  are shaded. Overlaid are the storm-relative streamlines. Plotted area is  $200 \times 160 \text{ km}$  with  $1 \text{ km}$  grid spacing. The origin of the grid is collocated with the CP4 radar.





**Figure 20c. 1152 UTC dual Doppler analysis of the vertical velocity field at 1.4 km Mean Sea Level (MSL). Contours are every  $5 \text{ ms}^{-1}$  with dashed lines depicting downdraft cores and shaded areas denoting updraft regions. Overlaid are the storm-relative streamlines. Plotted area is  $200 \times 160 \text{ km}$  with  $1 \text{ km}$  grid spacing. The origin of the grid is collocated with the CP4 radar.**



mesoscale outflow. This suggests that the location of new cell development has been influenced by the direction of the mesoscale outflow. The southern flank of the convective line is outside the dual-Doppler analysis domain. However, there is a southward directed outflow immediately behind the southernmost convective cells (between  $X = -50$  to  $-20$  for  $Y < -15$  in Fig. 20). At this time, this region of outflow appears to be more associated with the convective cells than the mesoscale region of stratiform rain farther to the north.

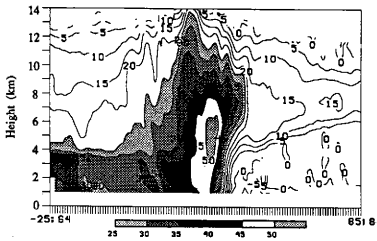
Comparison between the low-level flow and the vertical velocity fields (Fig. 20c) illustrates an important interaction between the meso- and convective scale outflows. The outflow from the convective downdrafts is embedded in the mesoscale outflow which apparently affects the direction in which the convectively generated cold pool can spread. The anticyclonically curving mesoscale outflow, opposing the environmental inflow in the central portion of the storm system, prevents the convective outflows from spreading backwards. This would result in the piling up of cold air behind the south-central and central portions of the leading convective line, as well as forcing this convective downdraft outflow to spread southward in along-line direction. At the same time, the cyclonically curving mesoscale outflow found in the northern portion of the system, does not appear to restrict the rearward spreading of the convective scale cold outflow.

An illustration of the along-line component of the outflow from convective downdrafts is the along-line current coincident with the leading convective line (Fig. 20a). The divergent region (located about  $X = 50$ ,  $Y = 65$  at 1152 UTC), found in a close proximity with the mesoscale divergence line, clearly separates southerly from northerly along-line flow. This suggests that the orientation of the along-line convective downdraft outflow is strongly affected by the interaction between the mesoscale outflow and the environmental kinematic field.

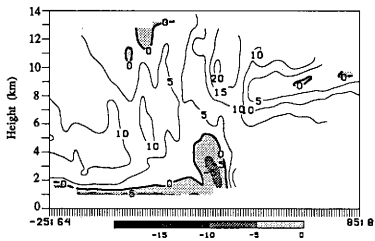
The interaction between the meso- and convective scale outflows is better illustrated in a vertical cross-section (1137 UTC), taken through the central portion of the convective line (Fig. 21). The storm-relative horizontal flow propagating in along-line direction (normal to the plane of the cross-section) is presented in the upper right panel. It illustrates a surprisingly deep, southward spreading flow, confined in a narrow area behind the leading convection. This flow represents the along line current, collocated with the convective line and detected in the horizontal cross-sections (Fig. 20). Comparison with the vertical velocity field (Fig. 21, lower left panel) indicates the

Figure 21. Vertical cross-section of reflectivity (upper-left panel), vertical velocity (lower-left panel), storm-relative horizontal flow in the along-line direction (upper-right panel) and storm-relative horizontal flow in the cross-line direction (lower-right panel) at 1137 UTC. The cross-section is located in the central portion of the squall line (location is marked by the X and Y coordinates of the end points, given at the two ends of the X axis) and oriented in direction, normal to the local orientation of the convective line (the horizontal axis is pointing towards  $117^\circ$  from true north). Distance along X axis is 123 km. Reflectivity is contoured every 5 dBz, starting at 5 dBz. Shaded are areas with reflectivity in excess of 25 dBz. Vertical velocity is contoured every  $5 \text{ ms}^{-1}$ , with dashed lines depicting the downdraft cores and shaded areas indicating the updraft regions. Along-line storm-relative flow component (normal to the plane of the cross-section) is contoured every  $5 \text{ ms}^{-1}$ . Shaded are negative values (flow out of the page), representing northerly flow. Cross-line storm-relative flow (component in the plane of the cross-section) is contoured every  $5 \text{ ms}^{-1}$ . Shaded are positive values (flow from left to right), depicting the rear-to-front component of the flow.

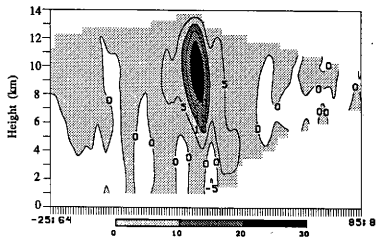
REFLECTIVITY AT 11:37 UTC



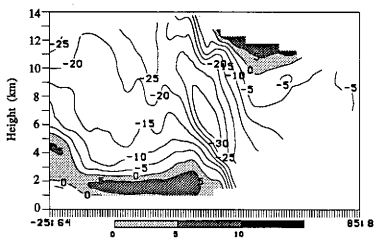
ALONG-LINE FLOW COMPONENT AT 11:37 UTC



VERTICAL VELOCITY AT 11:37 UTC



CROSS-LINE FLOW COMPONENT AT 11:37 UTC



convective outflow origin of this flow. A close examination of the structure of the two horizontal flow components, the along-line and the cross line component (tangential to the cross-section plane - lower right panel), reveals more details about the discussed scale interaction. The deep and extensive layer of surface RTF flow, mostly representing the mesoscale outflow, keeps the convective downdrafts from spreading rearward (note that FTR flow is not observed in the lowest levels as the two-dimensional conceptual model suggests). Thus, the convectively generated outflow must either deepen behind the convective line, surge forward as part of the rear-to-front flow, or surge outward in an along-line direction. From the analysis, it appears that a significant portion of the outflow is directed outward along the line, in the same along-line direction as the mesoscale outflow in which the convective downdraft outflow is embedded. Hence, the mesoscale circulation aids in the development of the deep layer of along-line convective outflow and affects its direction of propagation - the along-line flow is forced to spread northward in the northern flank, and southward in the central and south-central portions of the line. The southward along-line flow is confined to a narrow, but deep, channel which may affect the vertical orientation of the updrafts in the forward portion of the convective line. As noted by Weisman (1992) vertically oriented updrafts tend to be stronger than upshear tilted updrafts.

The location and structure of the central portion reflectivity cores (Fig. 20a) further illustrate the combined effect of the meso- and convective scale produced convergence. The northwest-southeast elongated reflectivity cores, observed in the central and south-central portions of the line, likely reflect the preferential growth of new cores on the southeast side of the old ones where convergence is enhanced by the southward spreading of the convective outflow. The steadiness of the reflectivity features in the central portion of the storm further illustrates the importance of convective-scale forcing (convection continuously redevelops in close proximity of the convective outflow from the strong old cells). In this case, the new cells form nearly adjacent to the mature older cells, similar to the "weak evolution" noted by Foote and Frank (1983). The location of this somewhat steady reflectivity core (found in the area where the mesoscale outflow is directly opposing the environmental inflow) illustrates the important effect of the mesoscale outflow on the strength of convective activity along the squall line.

The along-line variability in the mesoscale outflow with a strong rear-to-front component at low-levels is in stark contrast to the conceptual model (Fig. 18) where

only front-to-rear relative flow is indicated for low-levels between the heavy stratiform precipitation region and the convective line. It will be shown later that this mesoscale outflow is associated with the mesoscale downdraft in the rear-inflow branch of the cyclonic mesovortex. As such, the variability in the strength and orientation of the low level mesoscale outflow, and the associated variance in the convective outflow structure, may be the mechanism through which the cyclonic mesovortex affects the initial convective line of the MCS.

#### **Mid-to-Low Levels (2.4 to 3.9 km)**

At 3.4 km altitude strong front-to-rear flow was found throughout the convective region and extending rearward into the leading edge of the heaviest stratiform precipitation (Fig. 22a). Speeds in the FTR flow were maximum near the leading edge of the convection (Fig. 22b). Smull and Houze (1987a) showed a similar increase in FTR flow in the convective region and attributed the increase in wind speed to acceleration resulting from a low pressure perturbation found beneath sloping updrafts in the convective region (LeMone 1980, 1983). Near the leading edge of the strongest stratiform echo, the FTR current converged with the cyclonic circulation of the mesovortex. The center of the mesovortex was located behind the north-central portion of the system and slightly off the analysis domain (near  $X = -30$ ,  $Y = 85$  in Figs. 22a-c). While the mean vertical profile in the vortex area (Fig. 23) depicts 2 km altitude as the level of maximum relative vorticity, the flow field indicates that at this time the cyclonic circulation was best defined near the melting level (3.4 km). This discrepancy likely reflects the apparent backward tilt with height of the vortex center (at higher levels the vortex is out of the analysis domain) at this time.

Mean descent found at mid-to-low levels over the RTF branch of the mesovortex (Fig. 23) suggests that the outflow from the midlevel mesovortex is what was observed at lower levels. It is this descending branch of the cyclonic mesovortex (Fig. 22c) that affects the mesoscale outflow near the surface. Vertical advection of positive vorticity helps account for the cyclonic curvature of the outflow in the northern portion of the storm system. The low-level outflow in the central and southern portions of the storm system has a more characteristic anticyclonic curvature.

A specific example of the descending RTF flow is the reflectivity notch observed in the southern portion of the enhanced stratiform precipitation (near  $X = -10$ ,  $Y = 40$  in Fig. 22a). Its location suggests the entrainment of dry midlevel air by the RTF branch

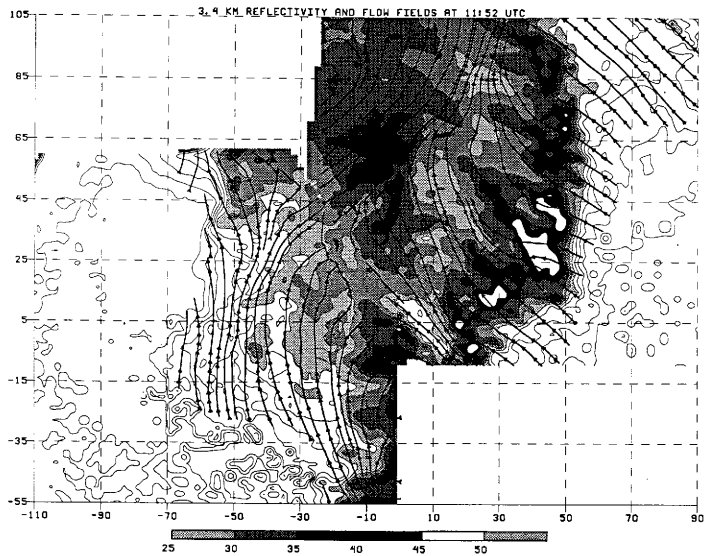


Figure 22a. As in Fig. 20a except for 3.4 km.



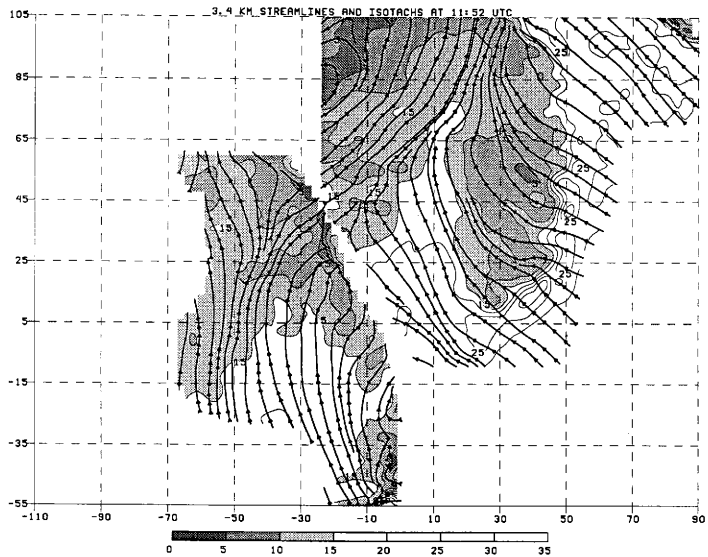


Figure 22b. As in Fig. 20b except for 3.4 km.

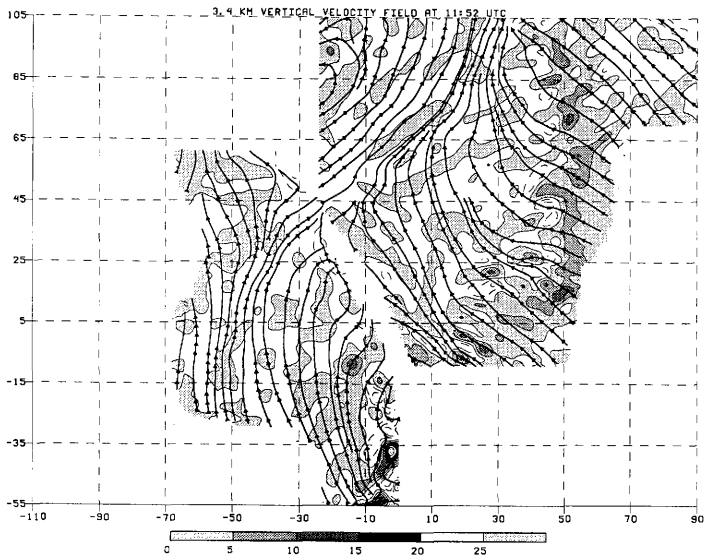


Figure 22c. As in Fig. 20c except for 3.4 km.

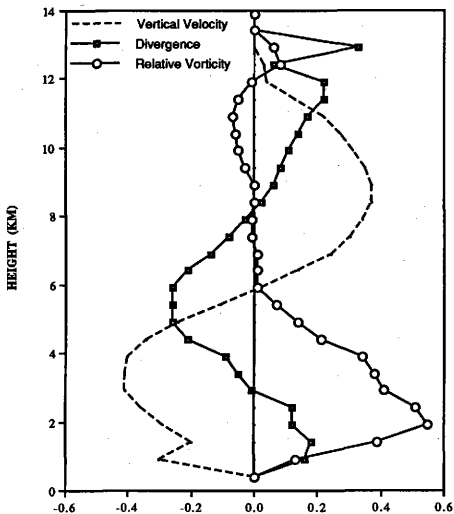


Figure 23. Vertical profile of the mean vertical velocity ( $ms^{-1}$ ), relative vertical vorticity ( $10^{-3}s^{-1}$ ) and divergence ( $10^{-3}s^{-1}$ ), averaged over the area of the midlevel vortex ( $-28 < X < 20$ ,  $59 < Y < 110$ ).

of the cyclonic mesovortex. As this drier air descends through the stratiform region, it is readily cooled by both evaporation and melting and represents a significant portion of the mesoscale cold pool observed at lower levels.

#### Mid-to-Upper Levels (4.4 to 8.9 km)

The closed cyclonic circulation is not observed above 4.4 km at 1152 UTC. Instead, as illustrated by the 6.9 km analysis (Fig. 24a), a broad region of FTR flow is found emanating from the northern portion of the convective region. A cyclonic circulation is implied in the streamline analysis (Fig. 24b) behind the central and southern portions of the convective line, but the vertical motion suggests that this apparent circulation consists of two separate mesoscale flow features - a descending rear-inflow and an ascending FTR flow (Fig. 24c). The interface between these two mesoscale flows is associated with area-average convergence and positive relative vorticity. Hence, the cyclonic curvature of the flow may increase with time, but at this altitude and at this time the air parcels are not trapped in a closed cyclonic circulation. Rather, the rear inflow branch of the circulation represents the vertical extension of the RTF branch of the mesovortex found at mid levels (Fig. 22 c). It is hypothesized that as the rear inflow descends toward the back of the convective line, the convergence of positive absolute vorticity acts to increase the cyclonic curvature of the parcel's trajectory and helps create the closed, or nearly closed, circulation observed at lower levels. Brandes (1990) makes a similar argument for the development of cyclonic mesovortex in another asymmetric squall line system.

The relatively strong rear-inflow (Smull and Houze 1987b) for the 28 May 1985 storm system may be a result of the favorable environmental wind profile. A strong west-northwesterly flow is observed between 6 - 10 km in the 00 UTC Topeka (not shown here) and Dodge City, Kansas soundings and also in the 12 UTC sounding from Oklahoma City, Oklahoma (Figs. 25a,b). These wind profiles indicate the presence of rear-inflow in the base-state environment. The RTF component of motion was likely increased through accelerations associated with the low pressure perturbations commonly found toward the rear of stratiform rain regions (e.g. Biggerstaff and Houze 1991a) and also underneath the slopping convective updrafts (LeMone 1983).

While the strength of the maximum rear-inflow at this level is likely related to the favorable base-state environment, the along-line variability of the strength and extent of the rear-inflow at this level appears to be more related to mesoscale storm dynamics than

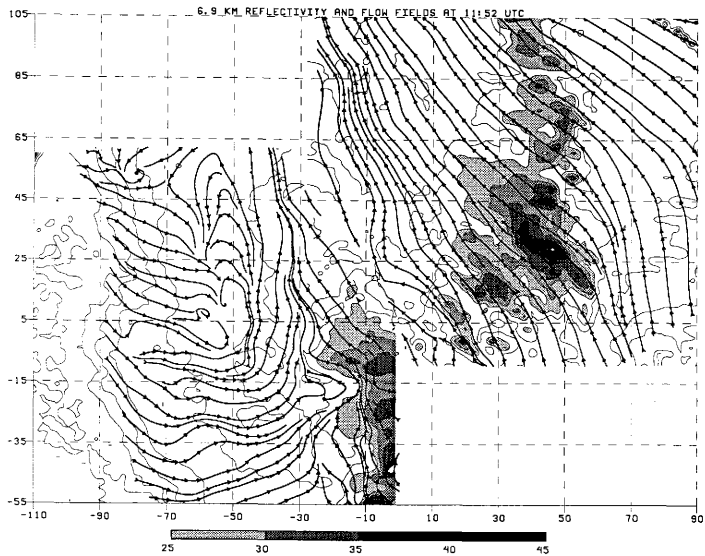


Figure 24a. As in Fig. 20a except for 6.9 km.

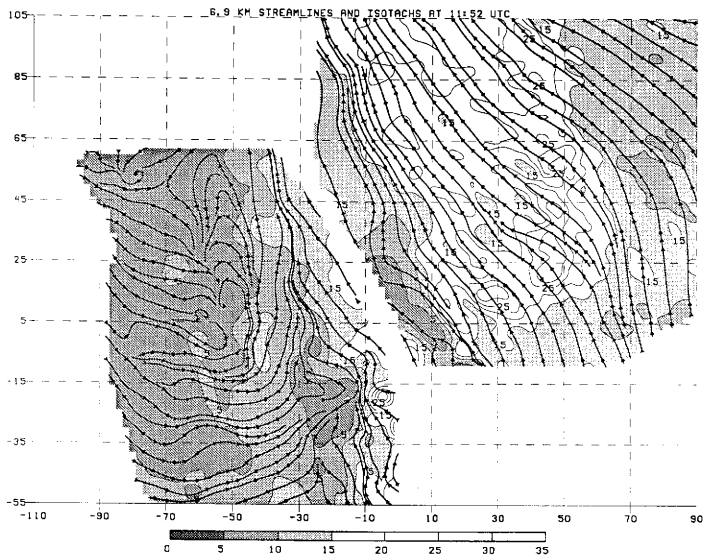


Figure 24b. As in Fig. 20b except for 6.9 km.

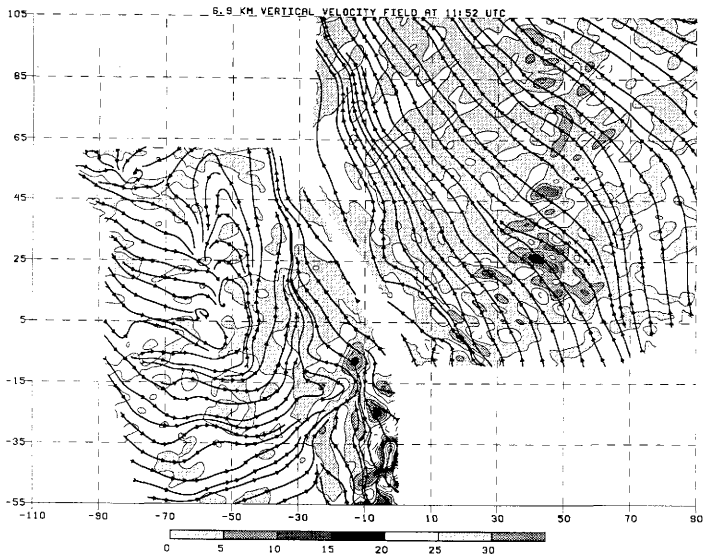


Figure 24c. As in Fig. 20c except for 6.9 km.

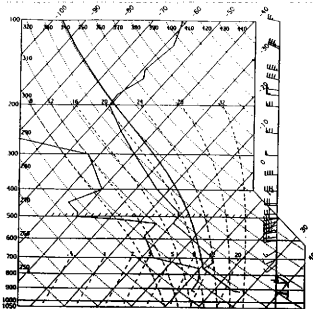


Figure 25a. Dodge City, Oklahoma (DDC) 0000 UTC 28 May 1985 skew T-log p profile of temperature, dewpoint temperature and wind (speed is in knots). Pressure is indicated in mb, temperature in °C. Plotted is also the trajectory of the lifted parcel, representing the averaged lowest 500 m. Lifting condensation level (LCL) is at 2439 m, level of free convection (LFC) is at 4010 m and equilibrium level (EQL) - at 12362 m.

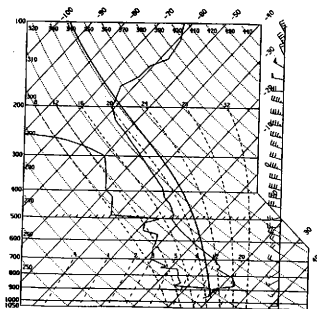


Figure 25b. As in Fig. 25a except for Oklahoma City, Oklahoma 1200 UTC. LCL is at 716 m, LFC - at 3728 m and EQL - at 12552 m.



an inherent feature of the base state environment. The broad FTR flow (hence a lack of RTF flow) in the northern portion of the storm system is consistent with detrainment from the more shallow convective updrafts in the northern flank of the convective line. While high spatial resolution sounding data are not available to firmly rule out the possibility of significant thermodynamic along-line gradients ahead of the storm system that could affect the overall storm structure as found by Barritt and Biggerstaff (1993) for the 10-11 June 1985 symmetric squall line system, inspection of low-level PPIs of "clear air" velocity data from the CP3 and CP4 radars suggests that significant differences in the low-level shear ahead of the storm did not exist, at least over the approximately 100 km scale covered by the Doppler radars. Surface mesonet data revealed a north-south oriented temperature gradient associated with the base-state environmental wind shear. This temperature gradient likely resulted in some along-line variability in the amount of convective available potential energy (CAPE; Moncrieff and Miller, 1976). But Weisman and Klemp (1982) tested the sensitivity of model storms to buoyancy and found only minor differences in updraft strength and depth for slight changes in CAPE. Moreover, the recent numerical simulation of Skamarock et al. (1993) was first conducted for a thermodynamically uniform base-state. Yet, their model asymmetric squall line still exhibited the same along-line variability in convective development as observed in the 28 May 1985 storm system. The broad FTR flow in the northern portion of the convective system at mid-to-upper levels is consistent with detrainment from the relatively shallow convective cells in that part of the storm system.

The vertical velocity field (Fig. 24c) illustrates in yet another way the along-line variability in convective activity. The strongest vertical velocities, with updraft cores in excess of  $35 \text{ ms}^{-1}$  are located on the southern flank of the system. Up- and downdraft intensity weaken northward, with an updraft maxima of  $15 \text{ ms}^{-1}$  observed in the central portion of the line, and only  $10 \text{ ms}^{-1}$  on the northern flank. Again, these features are consistent with the weaker, more shallow convective activity in the northern portion of the convective line where the mesoscale outflow contributed the least to the low-level convergence at the leading edge of the storm system.

#### Upper Levels (9.4 km and above)

Above 9.4 km, the flow field is dominated by FTR convective outflow throughout the analysis domain, except in the forward anvil of the storm. As illustrated by the 11.4 km dual-Doppler analysis (Figs. 26a-c), there is strong divergence associated

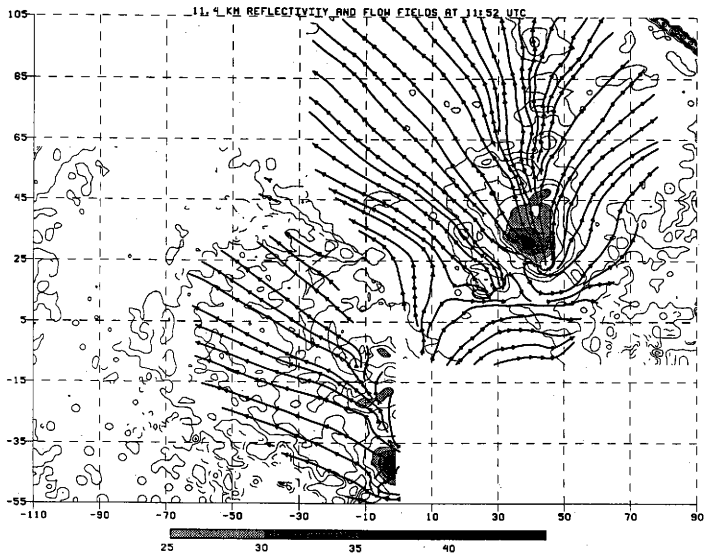


Figure 26a. As in Fig. 20a except for 11.4 km.

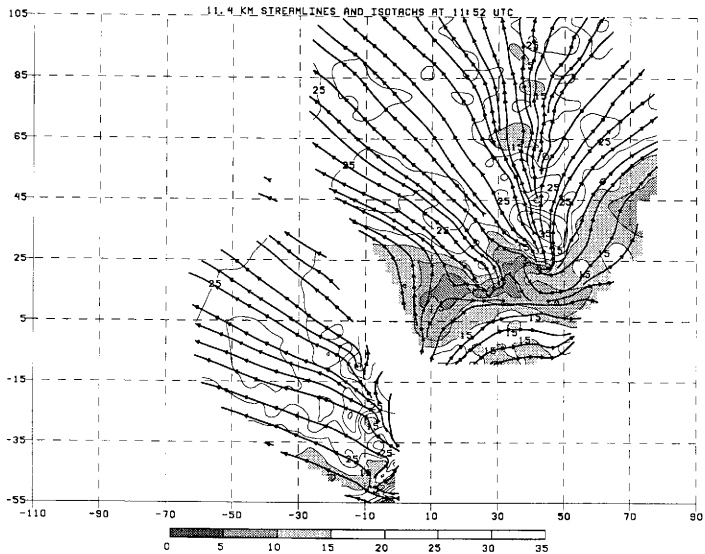


Figure 26b. As in Fig. 20b except for 11.4 km.

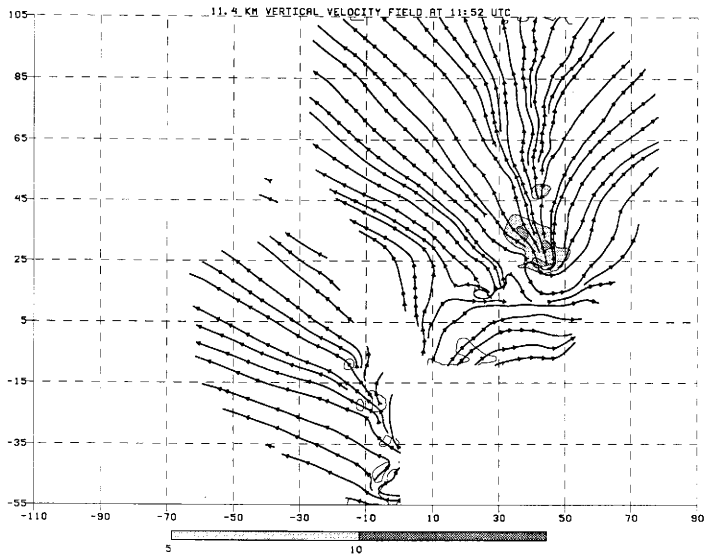


Figure 26c. As in Fig. 20c except for 11.4 km.

with the convective cells. The strong divergence coupled with the upper-level strong northwesterly environmental flow (Figs. 25a,b) is consistent with the RTF flow found in the extensive forward anvil of the storm system. Thorpe et al. (1982) found that increasing winds aloft were favorable for the development of extensive forward anvils.

At this time, the strongest updraft cores at upper levels were located near the central portion of the convective line (Fig. 26c). However, it is possible that equally strong or even stronger updrafts existed in the southern flank convection just outside of the dual-Doppler region. Regardless, the northern portion of the convective line, which was well shaped at this time, did not exhibit strong convective drafts at upper levels.

### Vertical Cross-Sections

Significant along-line variability in storm structure was noted in the horizontal cross-sections of all of the fields. Southern and central portions of the leading convective line were characterized by large, isolated reflectivity cores elongated in direction of storm propagation. At the same time, the northern flank was dominated by smaller, more closely spaced cores organized in a line perpendicular to the storm motion (Fig. 17 and 20). Strongest vertical drafts were preferably found on the southern flank of the system. The updrafts observed there were one-and-a-half times stronger than the ones found in the central portion of the line (Fig. 24c) and up to three times more intense than the northern flank updrafts. All this suggests the existence of three distinct regions along the convective line, with different convective characteristics. To summarize the vertical storm structure and illustrate the along-line variability, vertical cross-sections taken perpendicular to the local orientation of the convective line are presented. These vertical cross-sections allow for direct comparison to the two-dimensional conceptual model of squall line systems shown in Fig. 18. Moreover, the interaction between the low-level mesoscale outflow and the outflow from convective scale downdrafts is better illustrated by the vertical cross-sections.

#### Southern Flank

Given that the front edge of the convective line was outside the dual-Doppler analysis domain at 1152 UTC, we will use cross-sections at 1152 UTC (Fig. 27a) and 1125 UTC (Fig. 27b) to allow for better observation of the convective structure along the southern flank of the system. Both cross-sections are taken such that the horizontal axis is pointing towards 160° from true north.

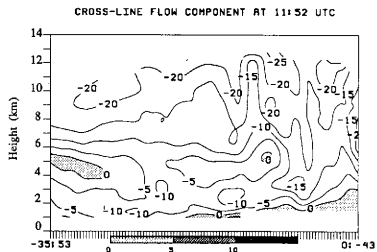
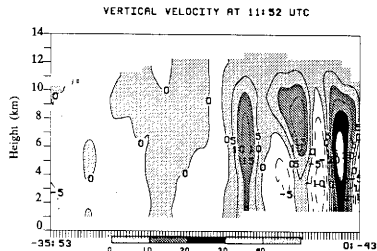
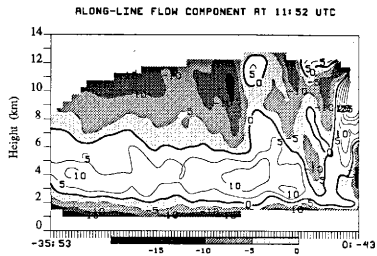
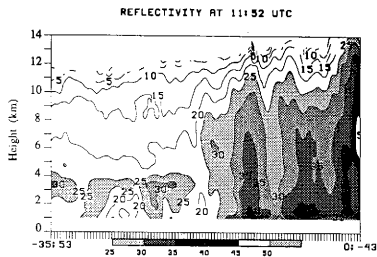


Figure 27a. As in Fig. 21 except the cross-section is taken through the southern portion of the storm at 1152 UTC. The X axis is pointing toward  $160^\circ$  from true north.

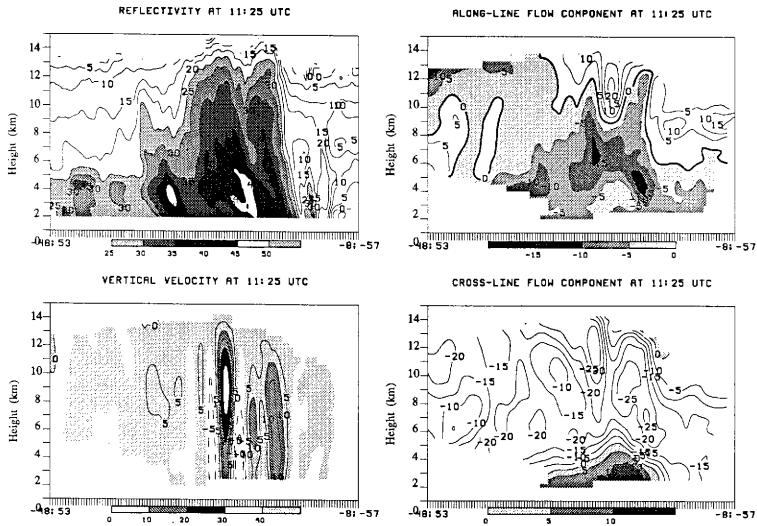


Figure 27b. As in Fig. 27a except for 1125 UTC.

Deepest reflectivity cores (although not necessarily highest intensity) were found in the southern flank of the convective line (Fig. 27a). This was also the region characterized by deep and intense vertical drafts, with updraft velocities greater than  $30 \text{ ms}^{-1}$  and downdrafts stronger than  $15 \text{ ms}^{-1}$ . Noteworthy is the vertical orientation of both updrafts and reflectivity cores (at 1152 UTC). Stratiform cloud, trailing to the northwest, was not very intense as compared to the other portions of the line (Fig. 28 and Fig. 29). Hence, in relative sense, processes of cooling through evaporation, melting or sublimation are not expected to have been of significant importance in the southern flank of the system. This may explain why the RTF flow, depicted by the cross-line storm-relative horizontal component, remained elevated (at 4 km altitude) to near the back of the convective line at 1152 UTC. As suggested earlier, this mid-to-upper level RTF flow illustrates the environmental mesoscale response to the entire convective ensemble. An area of convectively generated low-level RTF flow was found immediately beneath the leading convective line (Fig. 27b). Note that the observed flow structure suggests little if any contribution from the elevated RTF flow into the low level RTF flow. Hence, in this portion of the storm system, the mesoscale RTF flow apparently did not contribute significantly to the low-level cold pool near the leading edge of the convective line.

The along-line component of the flow depicts southwestward spreading convective downdrafts (Fig. 27a). It is speculated that this convective outflow, spreading south in an along-line direction, was mainly responsible for the southward expansion of convective activity discussed in the next chapter.

### *Central Portion*

While the deep and intense reflectivity cores found in the central portion of the storm were rather similar to the southern flank convection, the flow structure in the central portion was quite different (Fig. 28). Cross-line wind component reveals storm-relative RTF flow descending to the surface well behind the leading convective line. As already discussed, this roughly 2 km deep layer of RTF flow spreading along the surface for more than 50 km behind the convective line is not captured in the conceptual model of the squall-line systems (Fig. 18). Our study suggests that the current conceptual model which primarily reflects the structure of symmetric squall line systems, may not be representative for the asymmetric case. Indeed, the current conceptual model



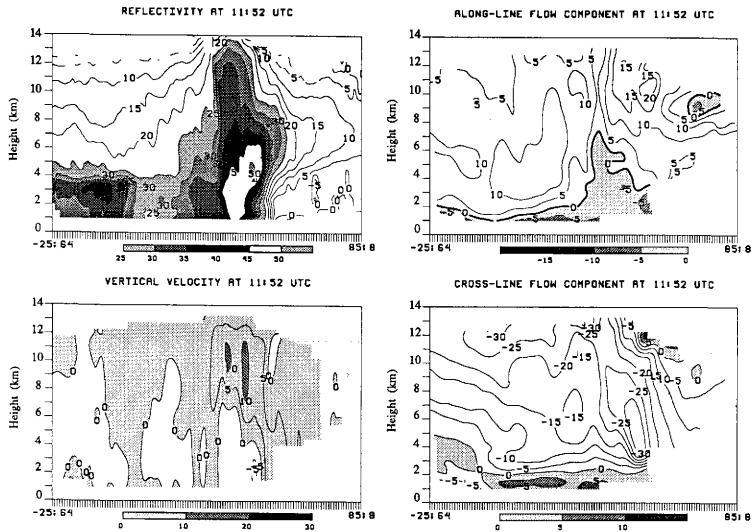


Figure 28. As in Fig. 21 except for 1152 UTC.

fails to identify the primary mechanism through which the mid-level mesovortex may affect the convective line.

Considering that the deep layer of surface RTF flow (assumed to represent the mesoscale cold pool) was likely unbalanced by the moderate shear environment, the deep and rather strong convection found in the central portion of the storm is unexpected in view of RKW theory. A numerical study by Weisman (1992) also concludes that RTF flow descending to the surface well behind the convective line will accentuate the upshear tilting process and weaken the storm system. The discrepancy between our case study and current theory may be explained in part by a vertical extension of convective forcing associated with the deep along-line band of southward spreading convective outflow which was confined to a narrow area behind the leading convection by the central portion mesoscale outflow. The enhanced low-to-midlevel forcing may help support the strong and rather vertical updrafts observed in the central portion of the convective line.

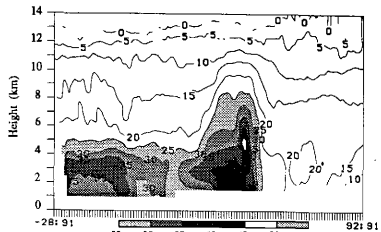
#### Northern Flank

Reflectivity and flow structure of the northern flank were distinctly different from those observed at the central and southern portions of the system (Fig. 29). Smaller and shallower reflectivity cores were associated with much weaker vertical drafts. Cross-line component of the storm-relative flow depicts a rather narrow current of very weak RTF flow, gently sloping toward the surface.

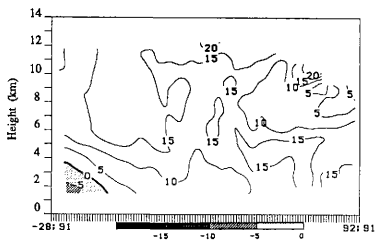
No southerly along-line flow was found on the northern flank of the storm. The northward spreading of the convective outflow in this portion of the storm is entirely attributed to the effect the northern flank cyclonically curving mesoscale outflow has on the direction of propagation of the embedded convective outflow (Fig. 20c). It is speculated that the weaker convective activity observed in the area resulted from the fact that northern flank meso- and convective scale outflows spread in direction parallel to the environmental flow, thus creating lesser low-level convergence as compared to the other portions of the convective line.

**Figure 29.** As in Fig. 21 except for the cross-section is taken through the northern portion of the storm at 1152 UTC. The X axis is pointing toward  $90^\circ$  from true north. Distance along the X axis is 110 km. Vertical velocities are contoured every  $2.5 \text{ ms}^{-1}$  with positive values shaded every  $5 \text{ ms}^{-1}$ .

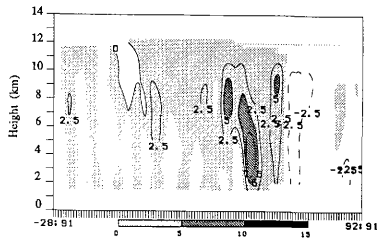
REFLECTIVITY AT 11:52 UTC



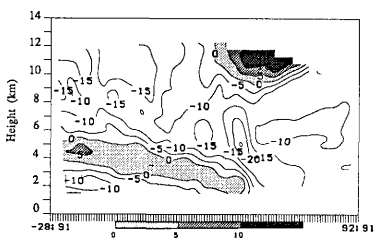
ALONG-LINE FLOW COMPONENT AT 11:52 UTC



VERTICAL VELOCITY AT 11:52 UTC



CROSS-LINE FLOW COMPONENT AT 11:52 UTC



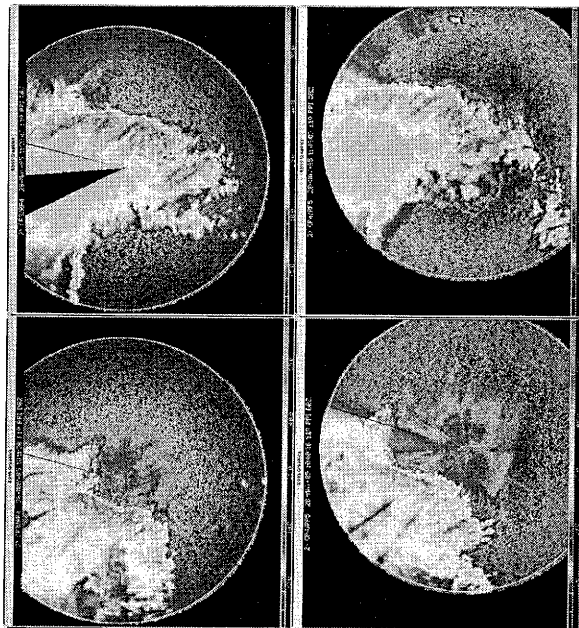
## CHAPTER VI

### STORM EVOLUTION

The 28th May squall line system moved through the PRE-STORM dual-Doppler analysis domain between approximately 1030 and 1310 UTC. During this period the storm underwent significant evolution as evidenced by the structure of the low-level reflectivity field (Fig. 30). Radar reflectivity at 1010 UTC (as seen by CP3 radar) illustrates the quasi-two-dimensional nature of the intense leading convective line at this time. Similar to the three-dimensional numerical simulation of Skamarock et al. (1993), the northern and southern ends of the line were slightly bowed forward. This is apparently characteristic of the early stage of the simulated asymmetric squall line system and represents the three-dimensionality of the flow interactions around the line ends. Even at this time, signs of developing asymmetry were observed in the structure of the stratiform precipitation region. An east-west oriented region of weak, isolated convective activity located on the southern flank of the system added to the asymmetry of the storm system.

The storm organization, observed one-and-a-half hours later was quite different. The total storm system had expanded and developed a highly three-dimensional storm structure. Repeated convection and advection of ice particles in the upper-level FTR flow led to a general intensification of the stratiform precipitation in the northern portion of the storm system, while progressive dissipation of stratiform echo was observed on the convective line's southern flank. The general character of the leading convection had also changed significantly. The south-central portion of the system had intensified with the southern flank extending southwest-northeast rather than east-west. Meanwhile, the intensity of the convective activity along the northern end of the convective line had decreased. In short, two-dimensionality observed earlier had diminished with the new convective organization characterized by isolated reflectivity cores, elongated in the direction of storm propagation and preferably located in the bowed out south-central portion of the storm. Thus, both dissipation of the stratiform precipitation in the southern portion of the system and the surging out and intensification of the southern flank convection contributed to the development of the asymmetric shape of the low-level radar reflectivity.

**Figure 30.** As in Fig. 17 except for a four panel plot presenting the reflectivity as seen by either CP3 or CP4 at four different time periods: upper-left panel - 1010 UTC low level reflectivity field as observed by the CP3 radar; lower-left panel - 1040 UTC reflectivity as seen by the CP4 radar; upper-right - 1120 UTC reflectivity as seen by CP3; and lower-right - 1148 UTC reflectivity as observed by CP4 radar.



### **Southern Flank (West Dual-Doppler Analysis Lobe)**

As noted before, the different segments of the system were observed during different time periods and for that reason the evolution of the southern and northern flanks of the system are discussed separately. Six dual-Doppler analyses over the southern portion of the system cover about 75 minutes of the storm system evolution (available are analyses at 1037, 1042, 1109, 1115, 1125, and 1152 UTC). Since the primary interest is in mesoscale features, the time resolution (5 to 27 minutes between analyses) is appropriate.

#### *Evolution of the reflectivity and low-level flow fields*

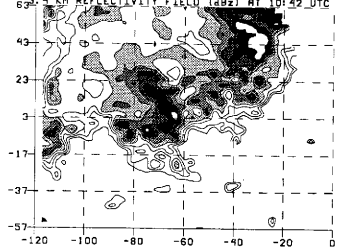
Presented here is the west lobe of the dual Doppler analysis domain which extended over the southernmost portion of the northeast-southwest oriented leading line and the moderate intensity band of convection along the southern flank of the system (Fig. 31). Attention is focused on the observed metamorphosis in this convective band as it passed through the west-lobe analysis domain.

Structural changes in the low-level convective organization are illustrated by the evolution of the 3.4 km reflectivity field (Fig. 31). At 1042 UTC isolated, variable intensity cells were organized in a 20 km wide east-west oriented band, running approximately between grid points  $-120 < X < -50$ . The band was embedded in a rather uniform weak intensity stratiform area. A more intense convective cell was centered near  $X = -30, Y = 43$ . This cell weakened between 1042 and 1109 UTC and then moved outside the dual-Doppler analysis domain. Another elongated high reflectivity core was centered at  $X = -70, Y = 8$ . As time progressed, the structure of this cell became more complex, revealing an ensemble of reflectivity cores. Storm intensity increased and the ensemble expanded in a northwest-southeast direction as new convection developed ahead of the old, preferably on the south-southeast end. This evolution is further illustrated by a sequence of 6.4 km reflectivity (Fig. 32) and 5.4 km vertical velocity fields (Fig. 33) which depict new reflectivity and updraft cores developing on the southern end in conjunction with a relative decrease in convective activity toward the north-northwest. Discrete propagation lead to south-southeast expansion of the convection and surge of the convective ensemble to where the ensemble became aligned with the northern portion of the convective line by 1152 UTC (Fig. 30, lower-right panel). Pronounced decrease in reflectivity in the immediate vicinity of the convective ensemble accompanied its intensification and south-southeastward

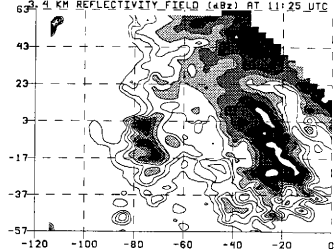


**Figure 31. Dual-Doppler constructed reflectivity field of the southern flank convection at 3.4 km altitude and four time periods: upper-left panel - 1042 UTC; lower-left - 1109 UTC; upper-right - 1125 UTC; lower-right - 1152 UTC. Reflectivity is contoured every 5 dBz, starting at 10 dBz. Shaded are areas with reflectivity in excess of 25 dBz. Plotted area is 120 x 120 km (with 1 km grid spacing) covering the west lobe of the dual-Doppler analysis domain.**

63.4 KM REFLECTIVITY FIELD (dBz) AT 10:42 UTC

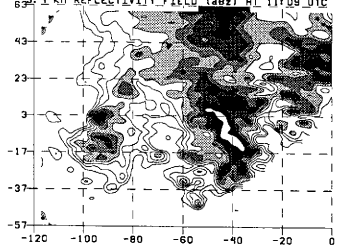


63.4 KM REFLECTIVITY FIELD (dBz) AT 11:25 UTC



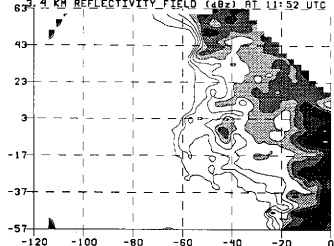
25

63.4 KM REFLECTIVITY FIELD (dBz) AT 11:09 UTC



25

63.4 KM REFLECTIVITY FIELD (dBz) AT 11:52 UTC



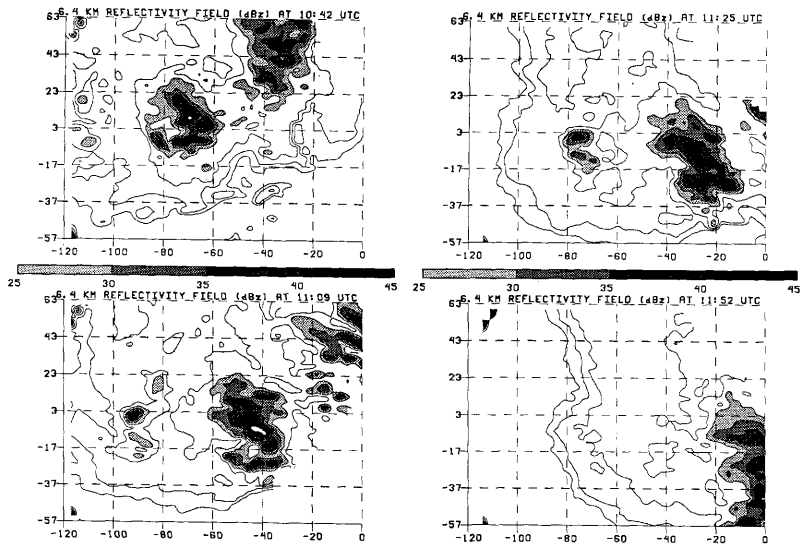


Figure 32. As in Fig. 31 except for 6.4 km.

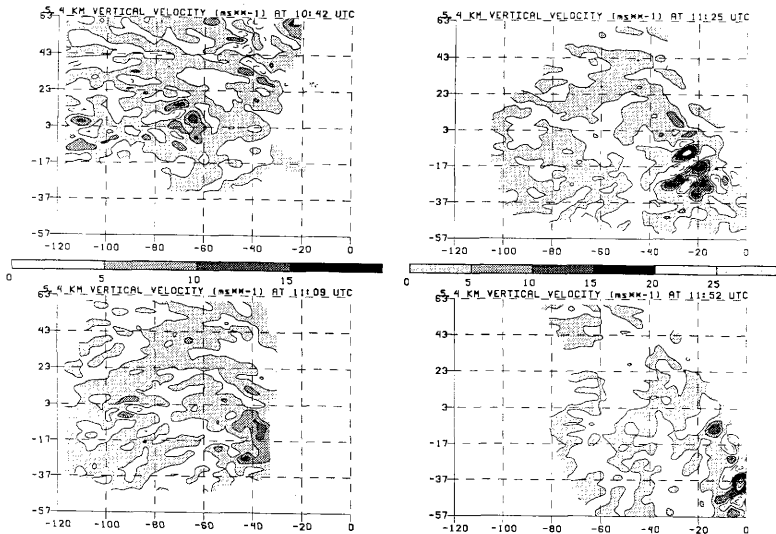


Figure 33. As in Fig. 31 except for 5.4 km vertical velocity field. Contours are every 5 ms<sup>-1</sup> with dashed lines depicting downdraft cores and shaded areas denoting updraft regions. Shading is every 5 ms<sup>-1</sup>.

expansion. By 1152 UTC this ensemble was the dominant feature of this portion of the storm system.

Observed structural changes in the reflectivity field are a manifestation of the flow evolution. At 1042 UTC the prominent feature of the 1.4 km wind field was the northerly mesoscale outflow which dominated the area behind the southern flank convective band (Fig. 34). The proximity of the stratiform precipitation region and scale of the divergent northerly flow coming from the heaviest stratiform rain region of the system indicate that the northerly flow was associated with outflow from the mesoscale downdraft. The extensive area of northerly flow generated an east-west oriented band of enhanced low-level convergence which apparently aided the initial development of convective activity along the observed east-west band on the southern flank of the storm system.

As time progressed the relative flow became more front-to-rear. Apparently as the isolated convective ensemble intensified, the convectively generated low-level outflow became the primary source of convergence which forced new development ahead and south-southeast of the old. Discrete propagation separated the leading edge from the mesoscale outflow and amplified the role of forcing by the convectively generated outflow. The much smaller scale of the convective outflow helps explain why only the growth of the isolated ensemble was stimulated.

By 1125 UTC, the only northerly flow in this region was associated with outflow from convective downdrafts (Fig. 35). Both available soundings (0000 UTC sounding from DDC and 1200 UTC sounding from OKC, Figs. 25a,b) show the level of free convection slightly below 4 km. This suggests that the southward spreading convectively generated outflow must have been very deep. As time progressed, the depth and intensity of the along-line flow increased, reflecting the additive contribution by all central and north-central convective outflows that were forced to spread southward by the low-level mesoscale flow.

#### Evolution of the upper-level flow

At the earlier time period (1042 UTC) the upper-level flow was dominated by FTR outflow from the convective cells. Some rear-to-front flow was found in the forward anvil and coming into the system around the southern end of the line (Fig. 36). Time and space consistency between observed reflectivity and maxima in the FTR flow (Fig. 37) leaves little doubt that low-level momentum transported upward by convection

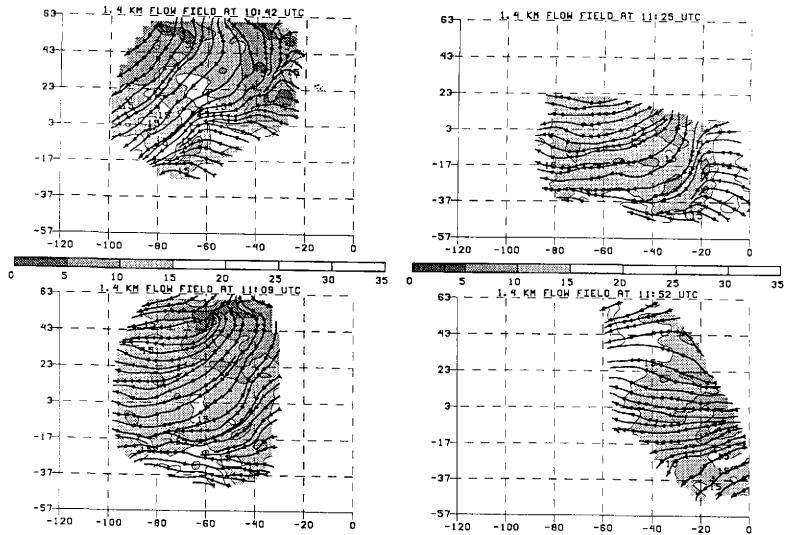


Figure 34. As in Fig. 31 except for 1.4 km flow field. Contoured and shaded is the storm-relative wind speed. Contours are every  $5 \text{ ms}^{-1}$  with shading depicting areas with speed  $< 15 \text{ ms}^{-1}$ . Overlaid are the storm-relative streamlines.

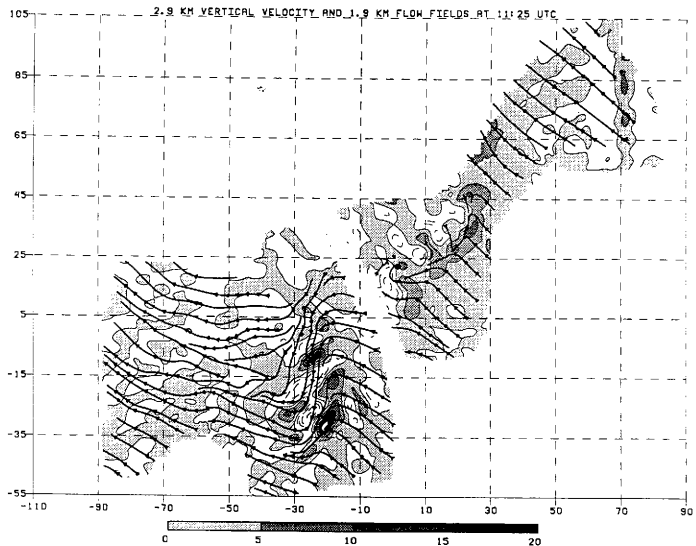


Figure 35. Dual-Doppler analysis of the west lobe flow field (120 x 120 km) at 1125 UTC. The 2.9 km vertical velocity field is contoured and shaded like in Fig. 33. Overlaid are the streamlines of the 1.9 km storm-relative horizontal flow field.

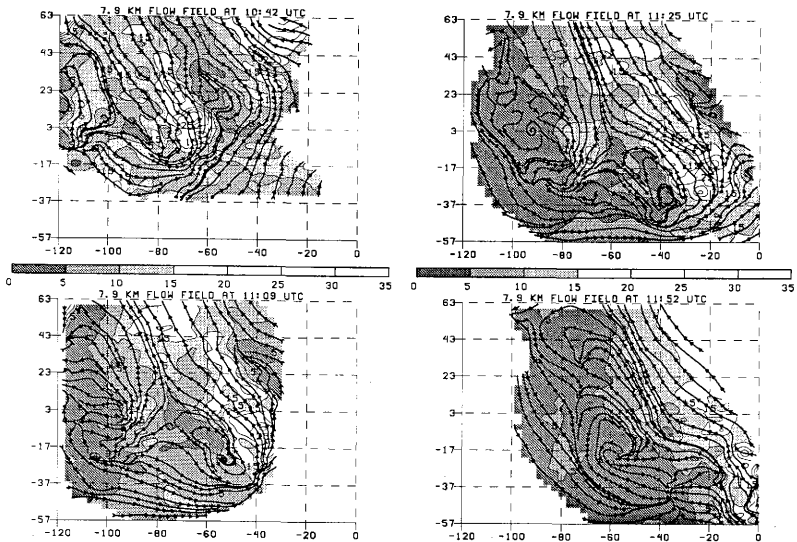


Figure 36. As in Fig. 34 except for 7.9 km.



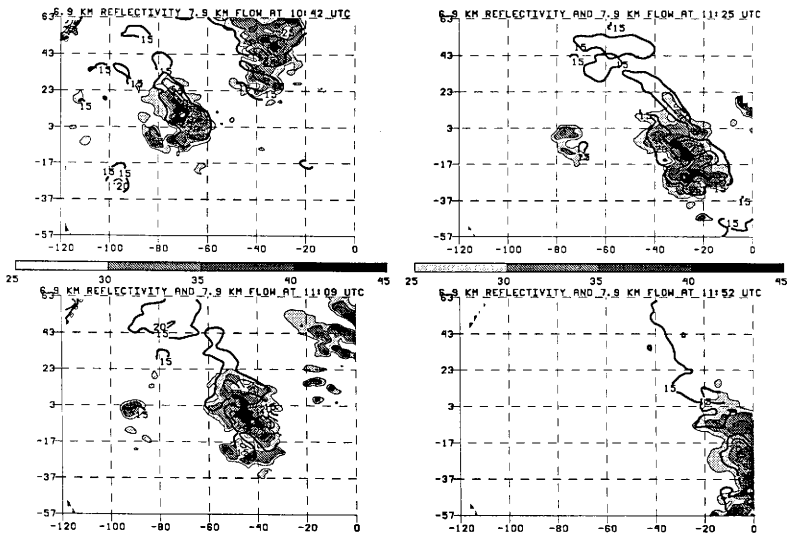


Figure 37. As in Fig. 31 except for 6.9 km reflectivity field (shaded are areas with reflectivity > 25 dBZ) and 7.9 km storm-relative horizontal speed field (bold contours encompass areas of wind speed > 15 ms<sup>-1</sup>).

was the source of the strong FTR flow found at upper levels. Indeed, the strength of the FTR flow near the leading line increased with the convection.

As time progressed, a RTF flow developed in response to the active convective ensemble along the southern end of the line. Both divergence from convective cells farther back and forward acceleration of the flow in response to the growing convective ensemble likely contributed to the development of the RTF flow in this region. Since the area covered by RTF flow increased as the rearward convective cells dissipated, most of the RTF momentum at the later times may have been a response to the growing convective ensemble and the remainder of the leading convective line. RTF flow was also observed at successively lower altitudes later in the analysis period. Smull and Houze (1987b) and Biggerstaff and Houze (1991a) discuss how RTF momentum develops in the stratiform precipitation region in response to pressure perturbations associated with the squall line system.

The distribution of RTF and FTR flow led to the initial development of cyclonic curvature in the wind field. More importantly, there was a band of convergence associated with the interaction of these two flows. As the area covered by RTF flow increased, the convergence region expanded. It is likely that the convergence of positive absolute vorticity contributed to the formation of a more coherent mesoscale vortex, present over a deeper layer of the troposphere as suggested by Brandes (1990) for a similar squall line system. However, development of a deep vortex over the southern portion of the convective line did not occur. The combination of FTR flow carrying cloud condensate north-northwestward and the influx of dry mid-level air in the RTF flow led to dissipation of the stratiform precipitation behind the southern flank of the convective line. With little stratiform precipitation, latent heating and cooling would be reduced which would likely reduce the thermodynamically induced mesoscale pressure perturbations needed to maintain the midlevel convergent circulation. As a result, a significant midlevel mesoscale circulation would be less likely to form along the southern portion of the storm system than the northern portion where enhanced stratiform precipitation (and the associated pressure perturbations) was found.

#### **North and Central Portions of the System (East Dual-Doppler Analysis Lobe)**

Four dual Doppler analyses covering the period 1125 to 1152 UTC provide better temporal resolution over the northern and central portions of the storm than that

available for the southern portion of the storm. Unfortunately, the observed period was shorter, 27 minutes compared to 75 minutes. Furthermore, the stratiform precipitation region was not well sampled by the earliest (1125 UTC) analysis (Fig. 38).

#### *Evolution of the convective structure and the low-level flow field*

Despite the short period of observation, significant changes in the structure of the convective line were observed. Pronounced weakening in the convective activity in the northern portion of the storm is evidenced by the reflectivity field (Fig. 38) in which there was a 5 dB decrease in reflectivity over the 27 minute analysis period. Using standard reflectivity-rainfall relationship (e.g. Battan 1973), a 5 dB decrease in reflectivity corresponds to a factor of 2 decrease in rainrate. The trend toward weaker convective activity was also well captured in the vertical velocity field. A significant decrease in updraft velocities between 1143 and 1152 UTC was observed (e.g. Fig. 39). In contrast, convective activity remained quite steady in the central portion of the convective line.

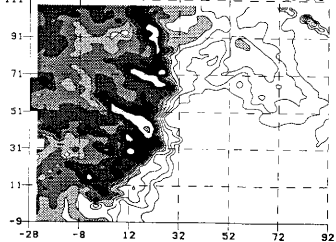
The structure and apparent movement of the convective cells also differed between the northern and central portion of the storm. In the north, the cells were smaller, more isolated, and had a more northward component of motion. In the central region, the cells were organized in an intense convective ensemble which was elongated in the direction of storm propagation and rather steady in shape and intensity throughout the 27 minute analysis period. Just to the southwest of the steady convective ensemble, the convective activity apparently increased with the > 45 dBz echo region expanding slightly.

While a 27 minute period is not long enough to make a general statement about the tendency of convection along the line, the 1310 UTC analysis ( Fig. 10) suggests that the northern portion of the line remained weak while the south-central portion continued to increase. The central portion remained rather steady. These trends in convective activity were likely associated with the interaction between the low-level mesoscale outflow and the environmental inflow (Fig. 40).

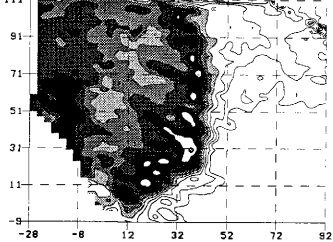
The along-line variability of the mesoscale outflow was discussed in the previous chapter. Cyclonic mesoscale outflow with a northward component in the northern portion of the system was directed parallel to the inflow and anticyclonic outflow in the central and southern portion of the system was directed nearly opposite the environmental inflow. During the 27 minute period sampled, this structure remained

**Figure 38. Dual-Doppler constructed reflectivity field of the central and northern portions of the convective line at 3.4 km altitude and four time periods: upper-left panel - 1125 UTC; lower-left - 1137 UTC; upper-right - 1143 UTC; lower-right - 1152 UTC. Reflectivity is contoured every 5 dBz, starting at 10 dBz. Shaded are areas with reflectivity in excess of 25 dBz. Plotted area is 120 x 120 km (with 1 km grid spacing) covering the east lobe of the dual-Doppler analysis domain. The origin of the grid is collocated with the CP4 radar.**

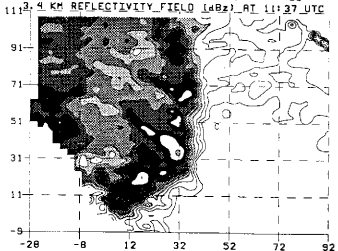
11:25 3.4 KM REFLECTIVITY\_FIELD (dBz) AT 11:25 UTC



11:43 3.4 KM REFLECTIVITY\_FIELD (dBz) AT 11:43 UTC



11:37 3.4 KM REFLECTIVITY\_FIELD (dBz) AT 11:37 UTC



11:52 3.4 KM REFLECTIVITY\_FIELD (dBz) AT 11:52 UTC

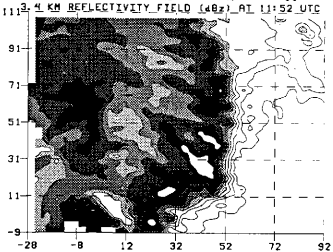
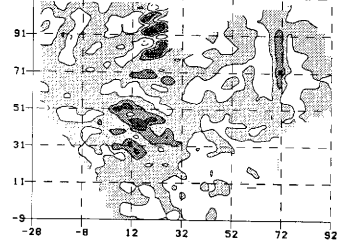
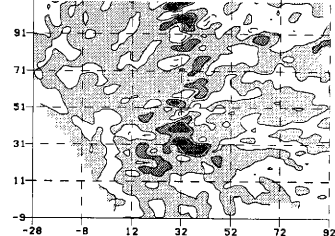


**Figure 39. Dual-Doppler constructed vertical velocity field of the central and northern portions of the convective line at 7.9 km altitude and four time periods: upper-left panel - 1125 UTC; lower-left - 1137 UTC; upper-right - 1143 UTC; lower-right - 1152 UTC. Contouring and shading are like in Fig. 33. Plotted area is 120 x 120 km (with 1 km grid spacing) covering the east lobe of the dual-Doppler analysis domain. The origin of the grid is collocated with the CP4 radar.**

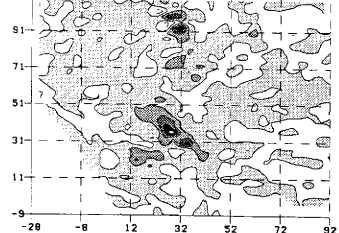
11:09 KM VERTICAL VELOCITY (ms<sup>-1</sup>) AT 11:25 UTC



11:09 KM VERTICAL VELOCITY (ms<sup>-1</sup>) AT 11:43 UTC



11:09 KM VERTICAL VELOCITY (ms<sup>-1</sup>) AT 11:37 UTC



11:09 KM VERTICAL VELOCITY (ms<sup>-1</sup>) AT 11:52 UTC

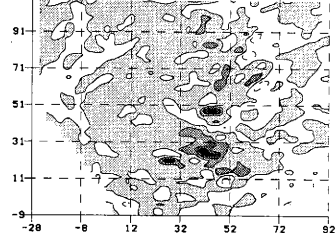
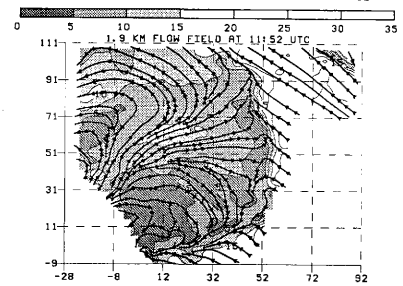
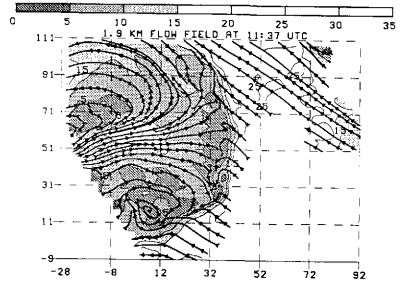
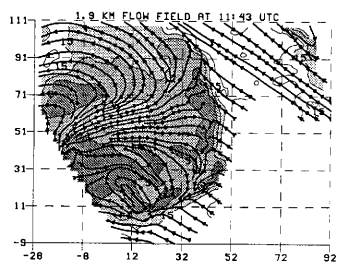
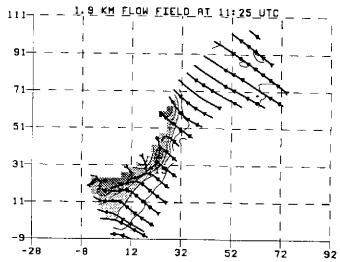


Figure 40. Dual-Doppler constructed storm-relative horizontal flow field of the central and northern portions of the convective line at 1.9 km altitude and four time periods: upper-left panel - 1125 UTC; lower-left - 1137 UTC; upper-right - 1143 UTC; lower-right - 1152 UTC. Contoured and shaded is the storm-relative wind speed with contour intervals and shading like in Fig. 35. Overlaid are the storm-relative streamlines. Plotted area is 120 x 120 km (with 1 km grid spacing) covering the east lobe of the dual-Doppler analysis domain. The origin of the grid is collocated with the CP4 radar.





relatively steady with only a slight tendency for stronger convergence in the south-central part of the line. With time, the mesoscale outflow in the area opposed more strongly the environmental inflow and apparently affected the intensity of the southward spreading convective outflows. Vertical cross-sections (Figs. 41a,b) illustrate the association between intensification in the along-line flow and the observed south-central convective development with time. The cross-sections also reveal the relationship between the along-line flow and the enhanced convergence in the across-line flow. The strong convergence was found ahead of the surface layer of RTF flow and was collocated with the leading edge of the southward-spreading flow. This further illustrates the important contribution of the convectively generated along-line outflow in forcing convergence at the leading line. Consistently preferred south-central location of the strongest surface convergence, depicted by the surface mesonet network (Fig. 19b), further describes the southward spreading combined meso- and convective outflows as one of the very important flow features, largely controlling the dynamics of this highly three-dimensional squall line system. This flow structure is consistent with the observed changes in the reflectivity field. The slightly stronger convergence in the south-central part of the storm likely led to the enhanced convective activity toward the end of the analysis period. The continued weak convergence along the northern part of the line may have been insufficient to generate significantly deep convective activity.

#### *Evolution of the upper-level flow*

Unlike the southern portion of the storm, no RTF flow was found at upper levels in the northern portion of the system (Fig. 42). Instead, highly divergent FTR flow was observed. The strongest divergence appeared to be located just ahead of the strongest upper-level reflectivity cores (Fig. 43). Enhanced FTR flow was associated with the convective cells. The region of strong FTR flow expanded southward in association with the convective development in the south-central portion of the system. Despite the decrease in low-level reflectivity in the northern part of the line, there was little change in the strength of the upper-level outflow.

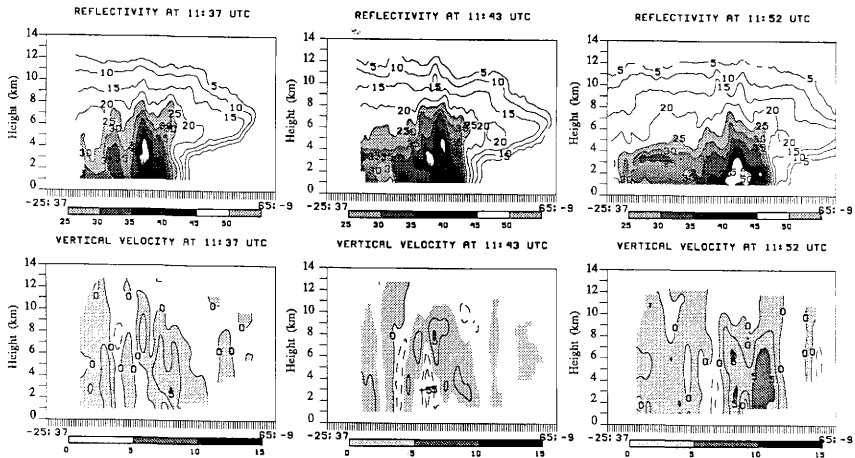


Figure 41a. Vertical cross-sections of reflectivity and vertical velocity fields at three time periods: 1137 UTC, 1143 UTC and 1152 UTC. The cross-sections are taken through the south-central portion of the storm system. The X axis is pointing toward  $117^\circ$  from true north. Distance along the X axis is 102 km. Reflectivity and vertical velocity are contoured and shaded like in Fig. 29.

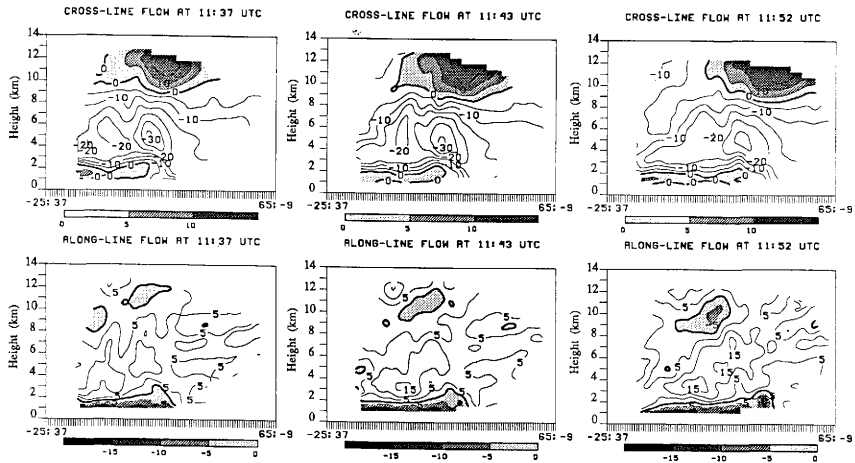


Figure 41b. As in Fig. 41a except for cross-line and along-line components of the storm-relative horizontal flow. Contouring and shading are like in Fig. 29.

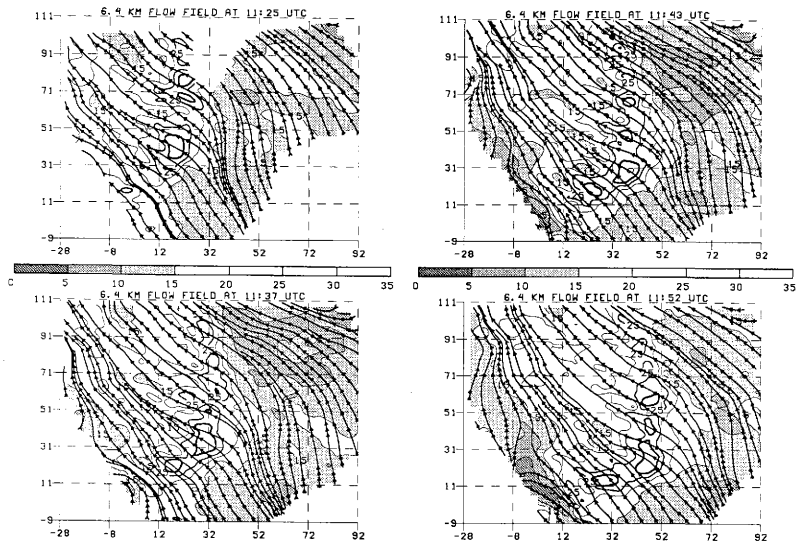


Figure 42. As in Fig. 40 except for 6.4 km. Bold lines depict cores of wind speed  $> 25 \text{ ms}^{-1}$ .

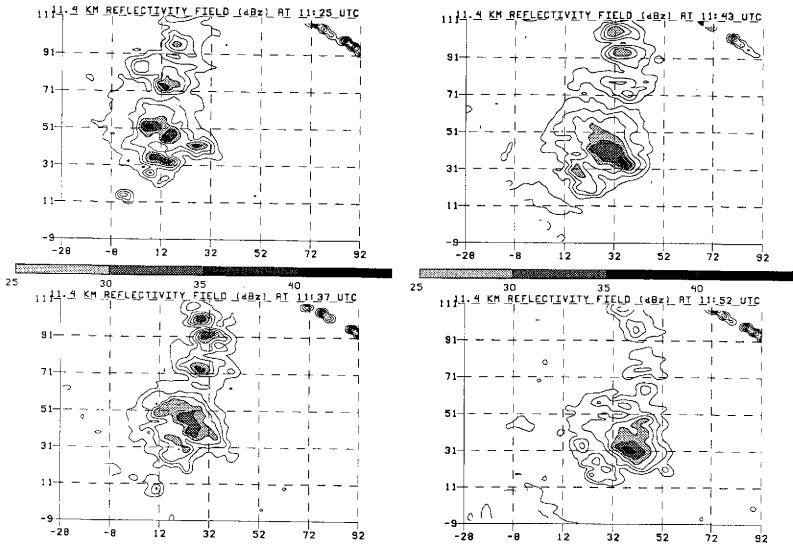


Figure 43. As in Fig. 38 except for 11.4 km.

## CHAPTER VII

### CONCLUSIONS AND RECOMMENDATIONS FOR FURTHER STUDY

Reflectivity and flow structure of the 28th May squall line system were highly four-dimensional. A transition from quasi-two-dimensional spatial structure to a well developed three-dimensional spatial structure was observed during the analyses period. Both evaporation of the stratiform precipitation behind the southern flank of the system and continuous southward expansion of convective activity contributed to the development of the asymmetric reflectivity pattern.

Dual-Doppler analyses of the flow field revealed the presence of a midlevel mesoscale cyclonic circulation, located in the stratiform area, trailing the north-central portion of the convective line. While low-to-midlevel (slightly above and below the melting level) mesovortex circulation was found during the entire observation period, a deep vertically oriented mesovortex was found only in the last analysis time (1308 UTC). This may have been the result of the circulation sloping with height such that the circulation was outside the analysis domain at the earlier time periods. Or, the mesovortex may have deepened with time through convergence of planetary and positive relative vorticity, consistently observed ahead and above the cyclonic circulation center. Interestingly, the area of cyclonic circulation was dominated by mesoscale descent at lower levels.

The southern, or rear-to-front, branch of the mesoscale cyclonic circulation was associated with the strongest mesoscale descent which indicated that dry midlevel air was entrained into the stratiform cloud and readily chilled by evaporation, sublimation and melting. The descending mesoscale outflow comprised a significant portion of the mesoscale cold pool found behind the leading convective line. Two distinct flow regimes (cyclonic northward flowing and anticyclonic southward flowing) characterized the low-level outflow. Along-line variability of the depth and direction of the mesoscale outflow implies that it contributed differently to the leading line convergence in the northern as compared to the central and southern portions of the convective line. Moreover, the northward and southward spreading mesoscale outflows affected very differently the structure and direction of propagation of the convective outflow, thus further accentuating the along-line variability of the leading-line convergence produced by the combined meso- and convective scale outflows.

The reflectivity structure also exhibited significant variability along the convective line. Larger, more isolated reflectivity cores, elongated in direction of storm propagation, were located in the southern and central portions of the storm, while northern flank convection was characterized by smaller, more closely spaced reflectivity cores which were organized in a line perpendicular to the storm propagation vector.

Deepest reflectivity cores and strongest vertical drafts were consistently found in the southern part of the convective line. In this portion of the storm an elevated storm-relative rear-inflow, almost reaching the back of the convective line, was associated with the deep convection. However, the elevated rear-to-front flow is perceived as a consequence and not a cause for the vertically oriented strong updrafts. Indeed, strong and deep convection was also observed in the central portion of the storm where the rear-to-front flow was confined to lower levels. It is suggested that the strong convective activity on the southern flank of the system was aided by the deep southward spreading convective outflow, confined by the anticyclonically curving mesoscale outflow in a narrow area behind the leading line. Southward spreading of the convective and mesoscale outflow led to the southward expansion of convective activity with time.

The northern portion of the line was characterized by the weakest convection. No southward convective outflow and a very weak rear-to-front flow, confined in a narrow layer, were associated with this portion of the line. Both across-line and along-line components of the flow suggested lesser leading line convergence as compared to the other areas of the storm.

As time progressed, northern flank convective activity decreased. At the same time the central portion of the convective line remained very active and the southern flank intensified significantly. The steady nature of reflectivity cores in the central and southern portion of the line, as well as their shape (elongated in direction of storm propagation) further illustrated the important interaction between the mesoscale and convective outflows which led to significant along-line variability in the forcing of new convective cells.

In summary, all of the observed parameters exhibited significant along-line variability on the scale of the mesovortex, illustrating a scale-interaction process. Presented hereafter is a new conceptual model (Fig. 44) reflecting the observed flow and scale interaction which we believe is fundamental to the structure of the mature asymmetric squall lines. The midlevel mesovortex, trailing the northern portion of the line is one of the fundamental features of the flow field. Associated with the midlevel



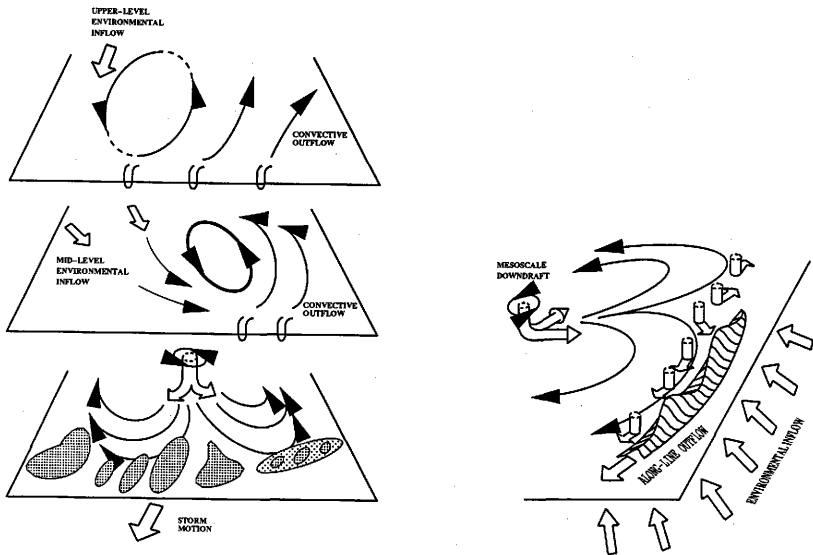


Figure 44. Conceptual model of the flow field of an asymmetric squall line system with an embedded midlevel mesovortex.

cyclonic circulation is a significant along-line variability in the structure of the mesoscale storm-relative horizontal flow. Primary mechanism by which the mesovortex affects the convective structure is by focusing the midlevel RI and altering the mesoscale low-level outflow: (i) in the northern portion of the system the mesoscale outflow is directed parallel to the environmental flow, thus creating less convergence; (ii) mesoscale outflow is strongly opposing the environmental inflow in the central and south-central portions of the storm, thus enhancing the convergence there; (iii) moreover, the altered low-level mesoscale outflow affects differently the direction of propagation of the embedded convective outflows, thus further accentuating the along-line variability of the storm-relative horizontal flow: convective outflows embedded in the northern-portion cyclonically curving mesoscale flow are free to spread both backward and northward, in direction almost parallel to the environmental inflow; at the same time, convective outflows embedded in the central and southern portion anticyclonically curving mesoscale flow, are forced to spread forward and southward, thus contributing to the production of the deep southward spreading along-line flow. This deep flow, confined in a narrow area co-located with the leading convective line, is viewed as the source for the enhanced convective forcing in the central and southern portions of the storm system as compared to the northern flank. Well pronounced along-line variability in the convective structure is associated with the observed variability in the pattern of combined meso- and convective scale low-level outflows. Stronger vertical updrafts and deeper reflectivity cores are consistently found in the southern and central portions of the system, where enhanced convergence was created by the system scale flow. Moreover, the observed along-line variability in the trends of convective evolution is explained in terms of the proposed scale interaction between the environmental inflow and the combined meso- and convective-scale outflows.

The numerical study by Skamarock et al. (1993) simulated an asymmetric squall line system with strikingly similar low-level flow and convective structure. The asymmetry of the system as well as the system's significant growth and migration to the south (right) of the original centerline were attributed to the effect of the Coriolis force. Their conceptual model is quite similar to ours, however it does not focus on the along-line variability of the mesoscale outflow, nor does it discuss the effect of this mesoscale outflow on the depth and direction of propagation of the convective outflows. The similarities between the two models, however, strongly suggest their applicability in the general case of the asymmetric squall-line systems.

To further the results of this study in determining the scale interaction between the mesovortex and the along-line convective variability, future work should focus on four main questions: (i) what is the contribution of the along-line  $\theta_e$  gradient in developing the convective variability along the line? (ii) do mature asymmetric storms always exhibit this type of along-line variability? (iii) is the distribution of severe weather, particularly damaging winds, associated with the scale interaction process illustrated in the conceptual model? (iv) can the increased depth of convective forcing, hypothesized in the conceptual model aid the longevity of the initial convective region by helping to maintain deep lifting needed to generate new convective cells in otherwise poor environmental conditions?

Additionally, more case-studies and numerical simulations should be analyzed to assess the general applicability of the proposed conceptual model of the scale interaction between the midlevel mesovortex and the along-line variability in structure and evolution of the parent convective line.

## REFERENCES

- Augustine, J.A. and K.W. Howard, 1988: Mesoscale Convective Complexes over the United States during 1985. *Mon. Wea. Rev.*, **116**, 685-701
- Barritt, R.C. and M.I. Biggerstaff, 1993: Kinematic Structure of a Long-Track Severe Straight-Line Wind Storm. *17th Conf. on Severe Local Storms*, St. Louis, Amer. Meteor. Soc., 577-581
- Battan, L.J., 1973: Radar Observation of the Atmosphere
- Biggerstaff, M.I. and R.A. Houze, Jr., 1991a: Kinematic and Precipitation Structure of the 10-11 June 1985 squall line. *Mon. Wea. Rev.*, **119**, 3034-3065
- \_\_\_\_\_, and \_\_\_\_\_, 1991b: Midlevel vorticity structure of the 10-11 June squall line. *Mon. Wea. Rev.*, **119**, 3066-3079
- Bosart, L.F. and F. Sanders, 1981: The Johnstown Flood of July 1977: A Long-Lived Convective System. *J. Atmos. Sci.*, **38**, 1616-1642
- Brandes, E.A., 1990: Evolution and structure of the 6-7 May 1985 mesoscale convective system and associated mesovortex. *Mon. Wea. Rev.*, **118**, 109-127
- Brown, J.M., 1979: Mesoscale unsaturated downdrafts driven by rainfall evaporation: a numerical study. *J. Atmos. Sci.*, **36**, 313-338.
- Carbone, R.E., M.J. Carpenter, and C.D. Burghart, 1985: Doppler Radar Sampling Limitations in Convective Storms, *J. Atmos. and Oceanic Tech.*, **2**, 357-361
- Chong, M., P. Amayenc, G. Scialom and J. Testud, 1987: A tropical squall line observed during the COPT81 experiment in West Africa. Part I: Kinematic structure inferred from dual-Doppler radar data. *Mon. Wea. Rev.*, **115**, 670-694
- Foote, G.B., and H.W. Frank, 1983: Case study of a hailstorm in Colorado. Part III: Airflow from triple-Doppler measurements. *J. Atmos. Sci.*, **40**, 686-707.
- Fovell, R.G., and Y. Ogura, 1989: Effect of vertical wind shear on numerically simulated multicell storm structure. *J. Atmos. Sci.*, **46**, 3144-3176.
- \_\_\_\_\_, 1991: Influence of the Coriolis force on two-dimensional model storms. *Mon. Wea. Rev.*, **119**, 606-630
- Fujita, T.T., 1955: Results of detailed synoptic studies of squall lines. *Tellus*, **7**, 405-436
- Gamache, J.F., and R.A. Houze, Jr., 1982: Mesoscale air motions associated with a tropical squall line. *Mon. Wea. Rev.*, **110**, 118-135

- \_\_\_\_\_, and \_\_\_\_\_, 1985: Further Analysis of the Composite Wind and Thermodynamic Structure of the 12 September GATE Squall Line. *Mon. Wea. Rev.*, **113**, 1241-1259
- Hamilton, R.A., and J.W. Archibold, 1945: Meteorology of Nigeria and adjacent territory. *Quart. J. Roy. Meteor. Soc.*, **83**, 303-314
- Houze, R.A., Jr., 1977: Structure and dynamics of a tropical squall line system. *Mon. Wea. Rev.*, **105**, 1540-1567
- \_\_\_\_\_, S.A. Rutledge, M.I. Biggerstaff, and B.F. Smull, 1989: Interpretation of Doppler weather radar displays of midlatitude mesoscale convective systems. *Bull. Amer. Meteor. Soc.*, **70**, No. 6, 608-619
- Klemp, J.B., 1987: Dynamics of tornadic thunderstorms. *Ann. Rev. Fluid Mech.*, **19**, 369-402
- Lafore, J.P., and M.W. Moncrieff, 1989: A numerical simulation of a midlatitude squall line in two dimensions. *J. Atmos. Sci.*, **46**, 521-544
- Leary, C.A., and E.N. Rappaport, 1987: The life cycle and internal structure of a mesoscale convective complex. *Mon. Wea. Rev.*, **115**, 1503-1527
- Lee, W.Ch., 1989: The Evolution and Structure of the Bow Echo/Microburst Events. *Univ. of California, Los Angeles, and National Center for Atmospheric Research, Cooperative Thesis No. 117*
- Leise, J.A., 1981: A Multidimensional Scale-Telescoped Filter and Data Extension Package. *NOAA Tech. Memo. ERL WPL-82*, Wave Prop. Lab., Boulder, Co., 22pp.
- LeMone, M.A., 1983: Momentum transport by a line of cumulonimbus. *J. Atmos. Sci.*, **40**, 1815-1834.
- \_\_\_\_\_, G.M. Barnes, and E.J. Zipser, 1984: Momentum fluxes by lines of cumulonimbus over the tropical oceans. *J. Atmos. Sci.*, **41**, 1914-1932.
- Maddox, R.A., 1980: Mesoscale convective complexes. *Bull. Amer. Meteor. Soc.*, **61**, No. 11, 1374-1387
- Marks, F.D., Jr., and R.A. Houze, Jr., 1987: Inner-core structure of Hurricane Alicia from airborne Doppler-radar observations. *J. Atmos. Sci.*, **44**, 1296-1317.
- McCann, D.W., 1981: The Enhanced-V, a Satellite Observable Severe Storm Signature. *NOAA Tech. Memo. NWS NSSFC-4*, National Severe Storms Forecast Center, Kansas City, Mo. (NTIS-#PB81-230328), 31pp.

- Moncrieff, M.W., and M.J. Miller, 1976: A theory for organized steady convection and its transport properties. *Quart. J. Roy. Meteor. Soc.*, **102**, 373-394
- Mohr, C.G., L.J. Miller, and R.L. Vaughn, 1979: An economical procedure for Cartesian interpolation and display of reflectivity factor data in three-dimensional space. *J. Appl. Meteor.*, **18**, 661-670.
- \_\_\_\_\_, and \_\_\_\_\_, 1983: CEDRIC - a software package for Cartesian space editing, synthesis, and display of radar fields under interactive control. Preprints, *21st Conf. on Radar Meteor.*, Edmonton, Amer. Meteor. Soc., 559-574
- Newton, C.W., 1950: Structure and mechanism of the prefrontal squall line *J. Meteor.*, **7**, 210-222
- Ogura, Y., and M.T. Liou, 1980: The structure of a midlatitude squall line. *J. Atmos. Sci.*, **37**, 553-567
- Oye, R., and R.E. Carbone, 1981: Interactive Doppler editing software. *20th Conf. Radar Meteor.*, Boston, Amer. Meteor. Soc., 683-689
- Rotunno, R., J.B. Klemp and M.L. Weisman, 1988: A theory for strong, long-lived squall lines. *J. Atmos. Sci.*, **45**, 463-485
- Skamarock, W.C., M.L. Weisman, J.B. Klemp, 1993: Three Dimensional Evolution of Simulated Long-Lived Squall Lines. *Submitted to JAS 7 May 1993*
- Smull, B.F., and R.A. Houze, Jr., 1985: A midlatitude squall line with a trailing region of stratiform rain: Radar and satellite observations. *Mon. Wea. Rev.*, **113**, 117-133.
- \_\_\_\_\_, and \_\_\_\_\_ 1987a: Dual-Doppler radar analysis of a midlatitude squall line with a trailing region of stratiform rain. *J. Atmos. Sci.*, **44**, 2128-2148
- \_\_\_\_\_, and \_\_\_\_\_ 1987b: Rear inflow in squall lines with trailing stratiform precipitation. *Mon. Wea. Rev.*, **115**, 2869-2889
- Thorpe, A.J., M.J. Miller, and M.W. Moncrieff, 1982: Two-dimensional convection in non-constant shear: a model of mid-latitude squall lines. *Quart. J. Roy. Meteor. Soc.*, **108**, 739-762
- Verlinde, J., and W.R. Cotton, 1990: A mesoscale vortex couplet observed in the trailing anvil of a Multicellular Convective Complex. *Mon. Wea. Rev.*, **118**, 993-1010
- Weisman, M.L. and J.B. Klemp, 1982: The Dependence of Numerically Simulated Convective Storms on Vertical Wind Shear and Buoyancy. *Mon. Wea. Rev.*, **110**, 504-520

- \_\_\_\_\_, 1992: The role of convectively generated rear-inflow jets in the evolution of long-lived mesoconvective systems. *J. Atmos. Sci.*, **49**, 1826-1847
- Zhang, D.L., and J.M. Fritsch, 1987: Numerical Simulation of the Meso- $\beta$  Scale Structure and Evolution of the Johns town Flood. Part II: Inertially stable warm-core vortex and the Mesoscale Convective Complex. *J. Atmos. Sci.*, **44**, 2593-2612
- \_\_\_\_\_, and \_\_\_\_\_, 1988: A Numerical Investigation of a Convectively Generated, Inertially Stable, Extratropical Warm-core mesovortex over Land. Part I: Structure and Evolution. *Mon. Wea. Rev.*, **116**, 2660-2687
- \_\_\_\_\_, and K. Gao, 1989: Numerical simulation of an intense squall line during 10-11 June 1985 PRE-STORM. Part II: Rear inflow and surface pressure perturbations. *Mon. Wea. Rev.*, **117**, 2067-2094.
- Zipsper, E.J., 1969: The role of organized unsaturated downdrafts in the structure and rapid decay of an equatorial disturbance. *J. Appl. Meteor.*, **8**, 799-814
- \_\_\_\_\_, 1977: Mesoscale and convective-scale downdrafts as distinct components of squall line circulation. *Mon. Wea. Rev.*, **105**, 1568-1589.

## V I T A

### SVETLA MIHAYLOVA HRISTOVA-VELEVA

#### E D U C A T I O N

- 1975            Graduated with golden medal (GPA - 4.0) from 7th Gymnasium "Georgi Dimitrov", Sofia, Bulgaria
- 1980            B.Sc. Degree in Physics with a specialization in Meteorology, SOFIA UNIVERSITY "Kliment Ohridski", Sofia, Bulgaria
- 1991 - 1994    Graduate student in the Department of Meteorology, Texas A&M University. Graduated with M.S. in May, 1994.
- 1992 - June    Participation in the Summer Colloquium on Observational Techniques in the Atmospheric Sciences - sponsored by NCAR.

#### E M P L O Y M E N T

- 1980 - 1988    Meteorologist - Department of Networks, Head Office of Hydrology and Meteorology, Bulgarian Academy of Science.
- 1989 - 1990    Research Assistant - Cooperative Institute for Applied Meteorological Studies, Texas A&M University.

#### F I E L D   P R O G R A M   E X P E R I E N C E

- 1992 - Spring    Radar operator during the CIAMS Spring '92 Doppler program.
- Dec. 1992        Radar operator on TOGA-radar during the international experiment TOGA-COARE.
- Jan. 1993

#### P R O F E S S I O N A L   M E M B E R S H I P S

American Meteorological Society, Chi Epsilon Pi

#### R E S E A R C H   A R E A S   O F   I N T E R E S T

Mesoscale Meteorology and Observational Techniques.

#### P E R M A N E N T   A D D R E S S

Department of Meteorology, Texas A&M University,  
College Station, TX 77843-3150

**Languages:** Bulgarian, English, Russian

**Computer Languages:** FORTRAN



Texas A&M University



R14818203520